B-meson production at forward and backward rapidity in p+p and Cu + Au collisions at √sNN=200 GeV

(PHENIX Collaboration) Aidala, C.; ...; Dumancic, Mirta; ...; Makek, Mihael; ...; Vukman, Nikola; ...; Zou, L.

Journal article, Published version
Rad u časopisu, Objavljena verzija rada (izdavačev PDF)

Permanent link / Trajna poveznica: https://urn.nsk.hr/urn:nbn:hr:217:601689

Download date / Datum preuzimanja: **2025-03-24**

Repository / Repozitorij:

Repository of the Faculty of Science - University of Zagreb

B-meson production at forward and backward rapidity in $p + p$ and Cu + Au collisions at $\sqrt{s_{NN}} = 200$ GeV

C. Aidala,[39,44] N. N. Ajitanand,[62,*] Y. Akiba,[57,58,†] R. Akimoto,[12] J. Alexander,[62] M. Alfred,[24] V. Andrieux,[44] K. Aoki,[32,57] N. Apadula,[29,63] H. Asano,[35,57] E. T. Atomssa,[63] T. C. Awes,[53] C. Ayuso,[44] B. Azmoun,[7] V. Babintsev,[25] A. Bagoly,[17] M. Bai,[6] X. Bai,[11] N. S. Bandara,[43] B. Bannier,[63] K. N. Barish,[8] S. Bathe,[5,58] V. Baublis,[56] C. Baumann,[7] S. Baumgart,[57] A. Bazilevsky,[7] M. Beaumier,[8] R. Belmont,[13,68] A. Berdnikov,[60] Y. Berdnikov,[60] D. Black,[8] D. S. Blau,[34] M. Boer,[39] J. S. Bok,[51] K. Boyle,[58] M. L. Brooks,[39] J. Bryslawskyj,[5,8] H. Buesching,[7] V. Bumazhnov,[25] C. Butler,[21] S. Butsyk,[50] S. Campbell,[14,29] V. Canoa Roman,[63] R. Cervantes,[63] C.-H. Chen,[58] C. Y. Chi,[14] M. Chiu,[7] I. J. Choi,[26] J. B. Choi,[10,*] S. Choi,[61] P. Christiansen,[40] T. Chujo,[67] V. Cianciolo,[53] Z. Citron,[69] B. A. Cole,[14] M. Connors,[21,58] N. Cronin,[45,63] N. Crossette,[45] M. Csanád,[17] T. Csörgő,[18,70] T. W. Danley,[52] A. Datta,[50] M. S. Daugherity,[1] G. David,[7,63] K. DeBlasio,[50] K. Dehmelt,[63] A. Denisov,[25] A. Deshpande,[58,63] E. J. Desmond,[7] L. Ding,[29] A. Dion,[63] D. Dixit,[63] J. H. Do,[71] L. D'Orazio,[42] O. Drapier,[36] A. Drees,[63] K. A. Drees,[6] M. Dumancic,[69] J. M. Durham,[39] A. Durum,[25] T. Elder,[21] T. Engelmore,[14] A. Enokizono,[57,59] H. En'yo,[57,58] S. Esumi,[67] K. O. Eyser,[7] B. Fadem,[45] W. Fan,[63] N. Feege,[63] D. E. Fields,[50] M. Finger,[9] M. Finger, Jr.,[9] F. Fleuret,[36] S. L. Fokin,[34] J. E. Frantz,[52] A. Franz,[7] A. D. Frawley,[20] Y. Fukao,[32] Y. Fukuda,[67] T. Fusayasu,[47] K. Gainey,[1] C. Gal,[63] P. Gallus,[15] P. Garg,[3,63] A. Garishvili,[65] I. Garishvili,[38] H. Ge,[63] F. Giordano,[26] A. Glenn,[38] X. Gong,[62] M. Gonin,[36] Y. Goto,[57,58] R. Granier de Cassagnac,[36] N. Grau,[2] S. V. Greene,[68] M. Grosse Perdekamp,[26] Y. Gu,[62] T. Gunji,[12] H. Guragain,[21] T. Hachiya,[57,58] J. S. Haggerty,[7] K. I. Hahn,[19] H. Hamagaki,[12] H. F. Hamilton,[1] S. Y. Han,[19] J. Hanks,[63] S. Hasegawa,[30] T. O. S. Haseler,[21] K. Hashimoto,[57,59] R. Hayano,[12] X. He,[21] T. K. Hemmick,[63] T. Hester,[8] J. C. Hill,[29] K. Hill,[13] R. S. Hollis,[8] K. Homma,[23] B. Hong,[33] T. Hoshino,[23] N. Hotvedt,[29] J. Huang,[7,39] S. Huang,[68] T. Ichihara,[57,58] Y. Ikeda,[57] K. Imai,[30] Y. Imazu,[57] J. Imrek,[16] M. Inaba,[67] A. Iordanova,[8] D. Isenhower,[1] A. Isinhue,[45] Y. Ito,[48] D. Ivanishchev,[56] B. V. Jacak,[63] S. J. Jeon,[46] M. Jezghani,[21] Z. Ji,[63] J. Jia,[7,62] X. Jiang,[39] B. M. Johnson,[7,21] K. S. Joo,[46] V. Jorjadze,[63] D. Jouan,[54] D. S. Jumper,[26] J. Kamin,[63] S. Kanda,[12,32] B. H. Kang,[22] J. H. Kang,[71] J. S. Kang,[22] D. Kapukchyan,[8] J. Kapustinsky,[39] S. Karthas,[63] D. Kawall,[43] A. V. Kazantsev,[34] J. A. Key,[50] V. Khachatryan,[63] P. K. Khandai,[3] A. Khanzadeev,[56] K. M. Kijima,[23] C. Kim,[8,33] D. J. Kim,[31] E.-J. Kim,[10] M. Kim,[61] M. H. Kim,[33] Y.-J. Kim,[26] Y. K. Kim,[22] D. Kincses,[17] E. Kistenev,[7] J. Klatsky,[20] D. Kleinjan,[8] P. Kline,[63] T. Koblesky,[13] D. Kotchetkov,[52] D. Kotov,[56,60] F. Krizek,[31] S. Kudo,[67] K. Kurita,[59] M. Kurosawa,[57,58] Y. Kwon,[71] R. Lacey,[62] Y. S. Lai,[14] J. G. Lajoie,[29] E. O. Lallow,[45] A. Lebedev,[29] D. M. Lee,[39] G. H. Lee,[10] J. Lee,[19,64] K. B. Lee,[39] K. S. Lee,[33] S. Lee,[71] S. H. Lee,[29,63] M. J. Leitch,[39] M. Leitgab,[26] Y. H. Leung,[63] B. Lewis,[63] N. A. Lewis,[44] X. Li,[11] X. Li,[39] S. H. Lim,[39,71] L. D. Liu,[55] M. X. Liu,[39] V-R Loggins,[26] V.-R. Loggins,[26] S. Lökös,[17,18] K. Lovasz,[16] D. Lynch,[7] C. F. Maguire,[68] T. Majoros,[16] Y. I. Makdisi,[6] M. Makek,[69,72] M. Malaev,[56] A. Manion,[63] V. I. Manko,[34] E. Mannel,[7] H. Masuda,[59] M. McCumber,[13,39] P. L. McGaughey,[39] D. McGlinchey,[13,20,39] C. McKinney,[26] A. Meles,[51] M. Mendoza,[8] B. Meredith,[26] W. J. Metzger,[18] Y. Miake,[67] T. Mibe,[32] A. C. Mignerey,[42] D. E. Mihalik,[63] A. Milov,[69] D. K. Mishra,[4] J. T. Mitchell,[7] G. Mitsuka,[58] S. Miyasaka,[57,66] S. Mizuno,[57,67] A. K. Mohanty,[4] S. Mohapatra,[62] P. Montuenga,[26] T. Moon,[71] D. P. Morrison,[7] S. I. M. Morrow,[68] M. Moskowitz,[45] T. V. Moukhanova,[34] T. Murakami,[35,57] J. Murata,[57,59] A. Mwai,[62] T. Nagae,[35] K. Nagai,[66] S. Nagamiya,[32,57] K. Nagashima,[23] T. Nagashima,[59] J. L. Nagle,[13] M. I. Nagy,[17] I. Nakagawa,[57,58] H. Nakagomi,[57,67] Y. Nakamiya,[23] K. R. Nakamura,[35,57] T. Nakamura,[57] K. Nakano,[57,66] C. Nattrass,[65] P. K. Netrakanti,[4] M. Nihashi,[23,57] T. Niida,[67] R. Nouicer,[7,58] T. Novák,[18,70] N. Novitzky,[31,63] R. Novotny,[15] A. S. Nyanin,[34] E. O'Brien,[7] C. A. Ogilvie,[29] H. Oide,[12] K. Okada,[58] J. D. Orjuela Koop,[13] J. D. Osborn,[44] A. Oskarsson,[40] G. J. Ottino,[50] K. Ozawa,[32,67] R. Pak,[7] V. Pantuev,[27] V. Papavassiliou,[51] I. H. Park,[19,64] J. S. Park,[61] S. Park,[57,61,63] S. K. Park,[33] S. F. Pate,[51] L. Patel,[21] M. Patel,[29] J.-C. Peng,[26] W. Peng,[68] D. V. Perepelitsa,[7,13,14] G. D. N. Perera,[51] D.Yu. Peressounko,[34] C. E. PerezLara,[63] J. Perry,[29] R. Petti,[7,63] M. Phipps,[7,26] C. Pinkenburg,[7] R. P. Pisani,[7] A. Pun,[52] M. L. Purschke,[7] H. Qu,[1] P. V. Radzevich,[60] J. Rak,[31] I. Ravinovich,[69] K. F. Read,[53,65] D. Reynolds,[62] V. Riabov,[49,56] Y. Riabov,[56,60] E. Richardson,[42] D. Richford,[5] T. Rinn,[29] N. Riveli,[52] D. Roach,[68] S. D. Rolnick,[8] M. Rosati,[29] Z. Rowan,[5] J. Runchey,[29] M. S. Ryu,[22] A. S. Safonov,[60] B. Sahlmueller,[63] N. Saito,[32] T. Sakaguchi,[7] H. Sako,[30] V. Samsonov,[49,56] M. Sarsour,[21] K. Sato,[67] S. Sato,[30] S. Sawada,[32] B. Schaefer,[68] B. K. Schmoll,[65] K. Sedgwick,[8] J. Seele,[58] R. Seidl,[57,58] Y. Sekiguchi,[12] A. Sen,[21,29,65] R. Seto,[8] P. Sett,[4] A. Sexton,[42] D. Sharma,[63] A. Shaver,[29] I. Shein,[25] T.-A. Shibata,[57,66] K. Shigaki,[23] M. Shimomura,[29,48] T. Shioya,[67] K. Shoji,[57] P. Shukla,[4] A. Sickles,[7,26] C. L. Silva,[39] D. Silvermyr,[40,53] B. K. Singh,[3] C. P. Singh,[3] V. Singh,[3] M. J. Skoby,[44] M. Skolnik,[45] M. Slunečka,[9] K. L. Smith,[20] M. Snowball,[39] S. Solano,[45] R. A. Soltz,[38] W. E. Sondheim,[39] S. P. Sorensen,[65] I. V. Sourikova,[7] P. W. Stankus,[53] P. Steinberg,[7] E. Stenlund,[40] M. Stepanov,[43,*] A. Ster,[70] S. P. Stoll,[7] M. R. Stone,[13] T. Sugitate,[23] A. Sukhanov,[7] T. Sumita,[57] J. Sun,[63] S. Syed,[21] J. Sziklai,[70] A. Takahara,[12] A Takeda,[48] A. Taketani,[57,58] Y. Tanaka,[47] K. Tanida,[30,58,61] M. J. Tannenbaum,[7] S. Tarafdar,[3,68,69] A. Taranenko,[49,62] G. Tarnai,[16] E. Tennant,[51] R. Tieulent,[21,41] A. Timilsina,[29] T. Todoroki,[57,67] M. Tomášek,[15,28] H. Torii,[12] C. L. Towell,[1] R. S. Towell,[1] I. Tserruya,[69] Y. Ueda,[23] B. Ujvari,[16] H. W. van Hecke,[39] M. Vargyas,[17,70] S. Vazquez-Carson,[13] E. Vazquez-Zambrano,[14] A. Veicht,[14] J. Velkovska,[68] R. Vértesi,[70] M. Virius,[15] V. Vrba,[15,28] N. Vukman,[72] E. Vznuzdaev,[56] X. R. Wang,[51,58] Z. Wang,[5] D. Watanabe,[23] K. Watanabe,[57,59] Y. Watanabe,[57,58] Y. S. Watanabe,[12,32] F. Wei,[51] S. Whitaker,[29] S. Wolin,[26] C. P. Wong,[21] C. L. Woody,[7] M. Wysocki,[53] B. Xia,[52] C. Xu,[51] Q. Xu,[68] L. Xue,[21] S. Yalcin,[63] Y. L. Yamaguchi,[12,58,63] H. Yamamoto,[67]

A. Yanovich,[25] P. Yin,[13] S. Yokkaichi,[57,58] J. H. Yoo,[33] I. Yoon,[61] Z. You,[39] I. Younus,[37,50] H. Yu,[51,55] I. E. Yushmanov,[34] W. A. Zajc,[14] A. Zelenski,[6] S. Zharko,[60] S. Zhou,[11] and L. Zou[8]

(PHENIX Collaboration)

[1]*Abilene Christian University, Abilene, Texas 79699, USA*
[2]*Department of Physics, Augustana University, Sioux Falls, South Dakota 57197, USA*
[3]*Department of Physics, Banaras Hindu University, Varanasi 221005, India*
[4]*Bhabha Atomic Research Centre, Bombay 400 085, India*
[5]*Baruch College, City University of New York, New York, New York, 10010 USA*
[6]*Collider-Accelerator Department, Brookhaven National Laboratory, Upton, New York 11973-5000, USA*
[7]*Physics Department, Brookhaven National Laboratory, Upton, New York 11973-5000, USA*
[8]*University of California-Riverside, Riverside, California 92521, USA*
[9]*Charles University, Ovocný trh 5, Praha 1, 116 36, Prague, Czech Republic*
[10]*Chonbuk National University, Jeonju 561-756, Korea*
[11]*Science and Technology on Nuclear Data Laboratory, China Institute of Atomic Energy, Beijing 102413, People's Republic of China*
[12]*Center for Nuclear Study, Graduate School of Science, University of Tokyo, 7-3-1 Hongo, Bunkyo, Tokyo 113-0033, Japan*
[13]*University of Colorado, Boulder, Colorado 80309, USA*
[14]*Columbia University, New York, New York 10027 and Nevis Laboratories, Irvington, New York 10533, USA*
[15]*Czech Technical University, Zikova 4, 166 36 Prague 6, Czech Republic*
[16]*Debrecen University, H-4010 Debrecen, Egyetem tér 1, Hungary*
[17]*ELTE, Eötvös Loránd University, H-1117 Budapest, Pázmány P. s. 1/A, Hungary*
[18]*Eszterházy Károly University, Károly Róbert Campus, H-3200 Gyöngyös, Mátrai út 36, Hungary*
[19]*Ewha Womans University, Seoul 120-750, Korea*
[20]*Florida State University, Tallahassee, Florida 32306, USA*
[21]*Georgia State University, Atlanta, Georgia 30303, USA*
[22]*Hanyang University, Seoul 133-792, Korea*
[23]*Hiroshima University, Kagamiyama, Higashi-Hiroshima 739-8526, Japan*
[24]*Department of Physics and Astronomy, Howard University, Washington, DC 20059, USA*
[25]*IHEP Protvino, State Research Center of Russian Federation, Institute for High Energy Physics, Protvino 142281, Russia*
[26]*University of Illinois at Urbana-Champaign, Urbana, Illinois 61801, USA*
[27]*Institute for Nuclear Research of the Russian Academy of Sciences, prospekt 60-letiya Oktyabrya 7a, Moscow 117312, Russia*
[28]*Institute of Physics, Academy of Sciences of the Czech Republic, Na Slovance 2, 182 21 Prague 8, Czech Republic*
[29]*Iowa State University, Ames, Iowa 50011, USA*
[30]*Advanced Science Research Center, Japan Atomic Energy Agency, 2-4 Shirakata Shirane,*
Tokai-mura, Naka-gun, Ibaraki-ken 319-1195, Japan
[31]*Helsinki Institute of Physics and University of Jyväskylä, P.O. Box 35, FI-40014 Jyväskylä, Finland*
[32]*KEK, High Energy Accelerator Research Organization, Tsukuba, Ibaraki 305-0801, Japan*
[33]*Korea University, Seoul 136-701, Korea*
[34]*National Research Center "Kurchatov Institute", Moscow 123098, Russia*
[35]*Kyoto University, Kyoto 606-8502, Japan*
[36]*Laboratoire Leprince-Ringuet, Ecole Polytechnique, CNRS-IN2P3, Route de Saclay, F-91128 Palaiseau, France*
[37]*Physics Department, Lahore University of Management Sciences, Lahore 54792, Pakistan*
[38]*Lawrence Livermore National Laboratory, Livermore, California 94550, USA*
[39]*Los Alamos National Laboratory, Los Alamos, New Mexico 87545, USA*
[40]*Department of Physics, Lund University, Box 118, SE-221 00 Lund, Sweden*
[41]*IPNL, CNRS/IN2P3, Univ Lyon, Université Lyon 1, F-69622 Villeurbanne, France*
[42]*University of Maryland, College Park, Maryland 20742, USA*
[43]*Department of Physics, University of Massachusetts, Amherst, Massachusetts 01003-9337, USA*
[44]*Department of Physics, University of Michigan, Ann Arbor, Michigan 48109-1040, USA*
[45]*Muhlenberg College, Allentown, Pennsylvania 18104-5586, USA*
[46]*Myongji University, Yongin, Kyonggido 449-728, Korea*
[47]*Nagasaki Institute of Applied Science, Nagasaki-shi, Nagasaki 851-0193, Japan*
[48]*Nara Women's University, Kita-uoya Nishi-machi Nara 630-8506, Japan*
[49]*National Research Nuclear University, MEPhI, Moscow Engineering Physics Institute, Moscow 115409, Russia*
[50]*University of New Mexico, Albuquerque, New Mexico 87131, USA*
[51]*New Mexico State University, Las Cruces, New Mexico 88003, USA*
[52]*Department of Physics and Astronomy, Ohio University, Athens, Ohio 45701, USA*
[53]*Oak Ridge National Laboratory, Oak Ridge, Tennessee 37831, USA*
[54]*IPN-Orsay, Univ. Paris-Sud, CNRS/IN2P3, Université Paris-Saclay, BP1, F-91406 Orsay, France*

[55]*Peking University, Beijing 100871, People's Republic of China*

[56]*PNPI, Petersburg Nuclear Physics Institute, Gatchina, Leningrad region 188300, Russia*

[57]*RIKEN Nishina Center for Accelerator-Based Science, Wako, Saitama 351-0198, Japan*

[58]*RIKEN BNL Research Center, Brookhaven National Laboratory, Upton, New York 11973-5000, USA*

[59]*Physics Department, Rikkyo University, 3-34-1 Nishi-Ikebukuro, Toshima, Tokyo 171-8501, Japan*

[60]*Saint Petersburg State Polytechnic University, St. Petersburg 195251, Russia*

[61]*Department of Physics and Astronomy, Seoul National University, Seoul 151-742, Korea*

[62]*Chemistry Department, Stony Brook University, SUNY, Stony Brook, New York 11794-3400, USA*

[63]*Department of Physics and Astronomy, Stony Brook University, SUNY, Stony Brook, New York 11794-3800, USA*

[64]*Sungkyunkwan University, Suwon 440-746, Korea*

[65]*University of Tennessee, Knoxville, Tennessee 37996, USA*

[66]*Department of Physics, Tokyo Institute of Technology, Oh-okayama, Meguro, Tokyo 152-8551, Japan*

[67]*Center for Integrated Research in Fundamental Science and Engineering, University of Tsukuba, Tsukuba, Ibaraki 305, Japan*

[68]*Vanderbilt University, Nashville, Tennessee 37235, USA*

[69]*Weizmann Institute, Rehovot 76100, Israel*

[70]*Institute for Particle and Nuclear Physics, Wigner Research Centre for Physics, Hungarian Academy of Sciences (Wigner RCP, RMKI)*
H-1525 Budapest 114, P.O. Box 49, Budapest, Hungary

[71]*Yonsei University, IPAP, Seoul 120-749, Korea*

[72]*Department of Physics, Faculty of Science, University of Zagreb, Bijenička c. 32 HR-10002 Zagreb, Croatia*

The fraction of J/ψ mesons which come from B-meson decay, $F_{B \to J/\psi}$, is measured for J/ψ rapidity $1.2 < |y| < 2.2$ and $p_T > 0$ in $p + p$ and Cu+Au collisions at $\sqrt{s_{NN}} = 200$ GeV with the PHENIX detector. The extracted fraction is $F_{B \to J/\psi} = 0.025 \pm 0.006$ (stat) ± 0.010(syst) for $p + p$ collisions. For Cu+Au collisions, $F_{B \to J/\psi}$ is 0.094 ± 0.028(stat) ± 0.037(syst) in the Au-going direction ($-2.2 < y < -1.2$) and 0.089 ± 0.026(stat) ± 0.040(syst) in the Cu-going direction ($1.2 < y < 2.2$). The nuclear modification factor, R_{CuAu}, of B mesons in Cu+Au collisions is consistent with binary scaling of measured yields in $p + p$ at both forward and backward rapidity.

I. INTRODUCTION

Heavy quarks (charm and bottom quarks in the context of this work) are a powerful tool to investigate initial-state effects and quark-gluon plasma (QGP) medium formation in heavy ion collisions. Initial-state nuclear effects can alter the number of heavy quarks produced compared to extrapolations from $p + p$ collisions. Once produced, however, the number of heavy quarks is preserved in strong interactions in the medium. Final-state effects, such as energy loss in the QGP [1,2], can only modify the momentum distribution of these quarks and open heavy mesons. On the other hand, the number of prompt J/ψ is not expected to be preserved in the medium because of the low $c\bar{c}$ binding energy, which can allow the J/ψ to be broken by medium interactions.

The B mesons, which decay to J/ψ and subsequently decay into dimuon pairs, represent a relatively clean channel to extract b-quark yields. At the Relativistic Heavy Ion Collider (RHIC), the PHENIX forward silicon-vertex detector (FVTX) along with the central silicon-vertex detector (VTX) provide the ability to measure precise event vertex positions as well as displacement of the decay muon trajectories from the reconstructed event vertex. This allows for the statistical separation of J/ψs from B-meson decays from prompt J/ψs. The PHENIX muon detector acceptance for B mesons in this channel is nearly constant over all transverse momenta, allowing for the direct extraction of momentum integrated b-quark yields, corresponding to the number of b quarks in the rapidity acceptance. With these yields, we can verify whether initial-state effects are relevant to B-meson production in nucleus + nucleus collisions.

The only known source of nonprompt J/ψ is production via B-meson decay [3], which has a typical decay time $\tau_0 \sim 1.5$–1.6 ps [4]. The constituent bottom quarks have mass $m_b \sim 4.5$ GeV/c^2 and are created from processes such as gluon fusion ($gg \to Q\bar{Q}$), flavor excitation where heavy quarks (Q) from the nucleon wave function scatter with gluons ($Qg \to Qg$), and gluon splitting ($gg \to Q\bar{Q}g$) [5,6]. Gluon-gluon fusion and flavor excitation are equally dominant, whereas the gluon splitting contribution is small at $\sqrt{s} = 200$ GeV according to PYTHIA8 hard scattering simulations [7].

Initial-state effects on the precursor gluons, before their hard scattering, include coherent multiple scattering, also called dynamical shadowing [6], incoherent multiple scattering [8,9], initial state energy loss [10], and saturation of small momentum fraction x gluons [11]. Nuclear parton distribution functions, extracted from deep inelastic scattering and Drell-Yan experimental data, such as EPS09 [12] and impact-parameter-dependent EPS09s [13], indicate a pattern of suppression for small-x gluons and an enhancement

---

*Deceased.

†akiba@rcf.rhic.bnl.gov

of intermediate to large-x gluons. Semileptonic decays of particles carrying heavy flavor and produced inclusively in $d + $ Au collisions at $\sqrt{s_{NN}} = 200$ GeV [14,15] indicate yield suppression at forward rapidity, where Bjorken $x \sim 5 \times 10^{-3}$ gluons dominate. The same analysis also revealed a clear yield enhancement at mid- and backward rapidity, where gluons with fractional momentum $0.05 \lesssim x \lesssim 0.2$ are dominant. A similar enhancement was observed in the measurements of D mesons in $d + $ Au at midrapidity [16].

Asymmetric Cu+Au collisions have the advantage of being a relatively large system that can access different x regions at positive and negative rapidities. Studies in these collisions provide a powerful test of how initial-state effects observed in small systems, such as $p + A$, can be projected in large heavy ion collisions. In the PHENIX muon arms, positive rapidity corresponds to the Cu-going direction, probing small-x in the Au nucleus and large-x in the Cu. Negative rapidity covers the Au-going direction, probing small-x in the Cu nucleus and large-x in the Au. Initial state parton distribution modifications are predicted to be stronger in the Au nucleus [17]. If these modifications have the same pattern as seen in $p(d) + $ A collisions, they may cause suppression in the Cu-going (positive rapidity) direction and enhancement in the Au-going direction. Initial-state energy loss [18] also results in larger suppression at positive rapidity.

In this study, we quantify the fraction of muons from the decay of nonprompt J/ψ in $p + p$ and Cu+Au collisions at $\sqrt{s_{NN}} = 200$ GeV using the PHENIX muon arms measuring in the rapidity range $1.2 < |y| < 2.2$. The nonprompt fractions are then used to calculate the nuclear modification of B mesons in Cu+Au collisions. This result uses the capability to measure the approach between muons and the collision vertex using the FVTX [19]. Section II describes the experimental apparatus and the data set. Section III describes the data selection, backgrounds, and defines the distance of closest approach (DCA_R). Section IV describes the simulation setup used to obtain the DCA_R distribution profiles. The fit to the real data distance of closest approach distributions is detailed in Sec. V. Systematic uncertainties are discussed in Sec. VI. Results and interpretations are presented in Sec. VII.

II. EXPERIMENTAL APPARATUS AND DATA SET

This analysis was performed using data sets obtained with the PHENIX detector (Fig. 1) at the Relativistic Heavy Ion Collider during the 2015 $p + p$ and 2012 Cu+Au $\sqrt{s_{NN}} = 200$ GeV runs. Each collision was identified by the north and south beam-beam counters (BBC) which each comprise 64 quartz radiators instrumented with mesh dynode PMTs covering charged particles in the pseudorapidity region $3.0 < |\eta| < 3.9$ and with time resolution of $\sim$50 ps. A fast online collision z vertex can be determined from the difference between the average north and south arrival times. A minimum-bias (MB) event is triggered by two or more hits in each BBC and a measured vertex position $|z_{\text{vtx}}| \lesssim 10$ cm, and results in an acceptance of $93 \pm 3\%$ of the total Cu+Au cross section. For $p + p$ collisions, one or more hits are required in each BBC for the MB trigger, and $55 \pm 5\%$ of the total inelastic cross section is accepted. This analysis also
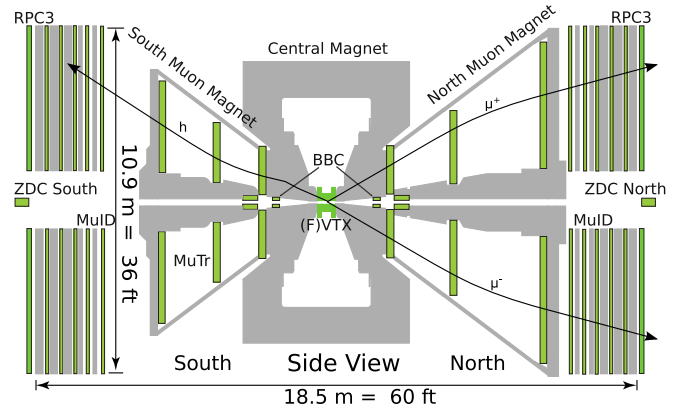

FIG. 1. Schematic view of the detector apparatus along with an illustrated dimuon and a hadron stopping in one of the muon identifier (MuID) gaps.

used a sample of dimuon triggered events (MUIDLL1_2D), which required two roads of hits found in the Iarocci tubes in the muon identifiers (MuID), including at least one road that reached the most downstream tubes.

A. PHENIX muon spectrometers

Each muon spectrometer covers a pseudorapidity range of $1.2 < |\eta| < 2.2$ and 2π in azimuth. Each spectrometer comprises hadron-absorber material, muon trackers (MuTr) inside a conical-shaped magnet, and a MuID. The first layer of hadron absorber, placed between the FVTX and the MuTr, comprises 19 cm of copper, 60 cm of iron from the central magnet, and 36.2 cm steel, corresponding to a total of 7.2 nuclear interaction lengths. This material absorbs pions and kaons emitted into the acceptance of the muon arms. The muon magnet system provides a radial field inside the MuTr volume of approximately $\int \mathbf{B} \cdot \mathbf{dl} = 0.72$ T m at 15 degrees from the beam axis, bending particles in the azimuthal direction.

Tracking and momentum measurements are performed by the MuTr, which comprises 8 octants of cathode strip chambers distributed in each of three z stations. The first two stations have three sensitive planes each, and the farthest station from the interaction region has two sensitive planes. Each plane contains two cathode readout strip planes with varying stereo angle orientations among the planes in the station to provide measurements in two spatial dimensions. The momentum resolution achieved by the MuTr is $\delta p / p \approx 0.05$ for a typical muon from J/ψ decays.

The north and south MuID systems are located downstream of the MuTr and comprise five absorber plates totaling 4.8 (5.4) nuclear interaction lengths in the south (north) arm. Two Iarocci tube planes with vertical and horizontal orientations distributed in six individual panels are placed after each of the five absorber gaps. Pion and kaon rejection after all absorber material is larger than a factor of 250. Only muons with momentum >3GeV/c are able to penetrate all absorbers. Recorded hits in the tubes are used to reconstruct roads which are used in the MUIDLL1_2D trigger and in full muon track reconstruction. Technical details of the muon arms can be found in Refs. [20,21].

TABLE I. Summary of FVTX geometry.

Mean z position of discs [cm]	$\pm 20.1, \pm 26.1, \pm 32.2, \pm 38.2$
ϕ segmentation each disk	48 wedges $\times$ 2 columns
Inner radius	4.4 cm
Strip pitch	75 μm
Strip length	3.4 mm to 11.5 mm
Total number of strips	1.08 M
Silicon thickness	320 μm

Particles produced at the primary vertex cross $\sim$7.2 interaction lengths of absorber before reaching the first MuTr station located at $z = \pm 190$ cm. Due to multiple scattering in the absorber, the projection of tracks reconstructed in the MuTr to the FVTX has a standard deviation radius of 3 cm. The FVTX helps track these particles from the absorber to the vertex point.

A precise vertex measurement is provided offline (Sec. III C) by the central arm vertex detector (VTX) and the FVTX. The VTX [22,23] is a silicon detector with four radial layers placed at 2.6, 5.1, 11.8, and 16.7 cm from the z axis, covering $2 \times \Delta\phi \approx 1.6\pi$ and $|z_{vtx}| < 10$ cm. The innermost two layers have pixel segmentation of $\Delta\phi \times \Delta z = 50$ μm $\times$ 425 μm and the two outer layers comprise stripixels with an effective pixel size of 80 μm in R$\Delta\phi$ and 1 mm in z.

The FVTX is a silicon detector installed in 2012 to precisely measure the radial distance of closest approach (DCA$_R$) of extrapolated particle trajectories to the collision vertex (Sec. III D), allowing statistical separation between prompt muons and muons from the decay of long-lifetime particles. Geometrical characteristics of the FVTX are listed in Table I. More technical details concerning the FVTX detector can be found in Ref. [19].

Tracks reconstructed in the silicon system are required to have at least three hits in different FVTX disks and/or VTX pixel layers (seen as half-cylinders in Fig. 2). The
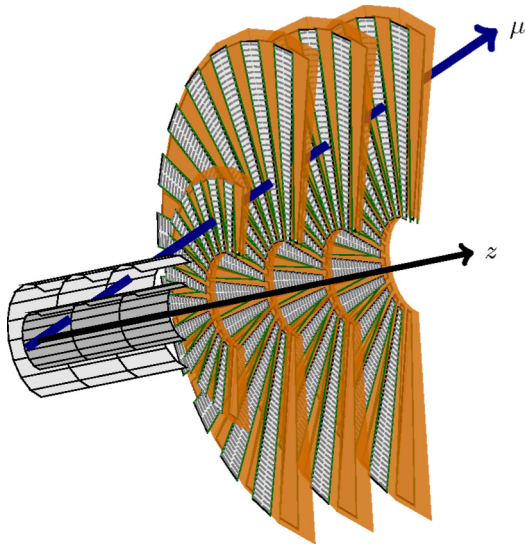

FIG. 2. Schematic view of the west VTX and north-west arm FVTX detectors used in this analysis.

magnetic field in the region of the FVTX is primarily in the z direction, resulting in only a very small bending of tracks in the ϕ direction. Therefore, the FVTX cannot measure particle momentum, which can be reconstructed only if the FVTX track is associated to a MuTr track.

B. Data set and quality assurance

Only collisions with a vertex determined by the VTX and FVTX within $z = \pm 10$ cm from the nominal interaction point are selected. Collisions where the vertex determination (Sec. III C) has an uncertainty larger than 500 μm (200 μm) are also rejected in $p + p$ (Cu+Au) data. The fraction of collisions within the vertex range used in this analysis is 14% in $p + p$ and 18% in Cu+Au. Only MB triggers or MUIDLL1_2D triggers in coincidence with a MB trigger (MUIDLL1_2D&MB) were analyzed. In $p + p$ the number of analyzed events in the selected vertex region is 3.4×10^{11}, corresponding to an integrated luminosity of $\int \mathcal{L} dt = 14.8$ pb^{-1}. In Cu+Au 5.7×10^9 MB and 284×10^6 MUIDLL1_2D&MB events were analyzed in the selected vertex range. The MB trigger is sensitive to $\sigma_{Cu+Au} = 5.23 \pm 0.15$ b of the total Cu+Au cross section, according to Glauber calculations reported in Ref. [17]. Therefore, the Cu+Au events used in this analysis correspond to $\int \mathcal{L} dt = 1.0$ nb^{-1}, or the $p + p$ equivalent of 11.8 pb^{-1}.

The run-by-run average DCA$_R$ (described in Sec. III D) measured for of all charged particles by the FVTX was found to be stable throughout the data collection period in the Cu+Au run. For the case of $p + p$ collisions, $\sim$10% of data are rejected due to instabilities of the measured DCA$_R$.

III. DATA SELECTION AND HOW TO OBTAIN THE DISTANCE OF CLOSEST APPROACH DISTRIBUTIONS

B mesons have a mean decay length $c\tau_0 \sim 450$ μm, a scale measurable by precision vertex detectors. At large rapidity the momentum boost $\gamma = \sqrt{p_z^2 + p_T^2 + m^2}/m$ to the decay length is larger than at midrapidity ($p_z \sim 0$), allowing *B*-meson identification via nonprompt decays even at zero transverse momentum.

Typically, the fraction of *B*-meson decays in J/ψ samples (here defined as $F_{B \to J/\psi}$) is determined by measuring the vertex given by the intersection of the two muon trajectories in the dimuon pair. This approach is not used in this analysis because: (1) the J/ψ dimuon vertex cannot be precisely determined because of the limited ϕ resolution of the FVTX; (2) a fraction of the sample of J/ψ decays would be lost in the sample when one of the muons reconstructed by the MuTr does not match to the FVTX.

In this analysis, the J/ψ decay is identified by the dimuon invariant mass of selected MuTr + MuID tracks. In a second step, muon candidates from the identified J/ψ decay that have matching FVTX tracks are selected. The radial distance of closest approach DCA$_R$ (Sec. III D) is determined for combined FVTX + MuTr + MuID tracks after quality cuts. The following sections detail how the sample is selected, how the backgrounds are treated, and how DCA$_R$ is defined.

A. Selection of J/ψ candidates

Single muon candidates are MuTr tracks that are associated to MuID roads (Sec. II A). The MuTr track is required to have at least 11 out of a maximum of 16 hits in different cathode planes, and the fitted track should return a $\chi^2/\mathrm{NDF} < 10$, cut based on the distribution obtained from simulated muons which also accounts for tracks crossing malfunctioning channels in the MuTr. Because a track is required to cross all absorbers, only muons with a total reconstructed momentum larger than $3\,\mathrm{GeV}/c$ are accepted. The MuID roads are required to have at least 6 out of a possible 10 hits in different tube planes, including a hit in one of the planes located behind the last MuID absorber. Three standard deviation cuts are applied to the distance and angle between the MuTr track and the MuID road projections at the first MuID gap. Dimuon pairs formed from MuTr + MuID selected muons are required to have an opening angle larger than $45°$ if the dimuon p_T is smaller than 5 GeV/c. Implementation of this cut helps remove contributions from ghost tracks. A fit involving the muon pair tracks and the collision vertex is required to have a $\chi^2/\mathrm{NDF} < 5(3)$ in $p+p$ (Cu+Au) data, corresponding to a maximum distance between the dimuon crossing and the collision point of approximately 1 cm. This cut has no impact on B decay acceptance.

Dimuon spectra in the region of the J/ψ mass are shown in Fig. 3 for both muon arms. The combinatorial background, shown as open circles in Figs. 3(a) and 3(b), corresponds to random combinations of muons. This background is determined from mixed-event dimuons and normalized by the geometric average between same-event like-sign sources N_{++}^{same}, N_{--}^{same} and mixed-event like-sign sources N_{++}^{mix}, N_{--}^{mix}:

$$\mathrm{Norm_{CB}} = \frac{\sqrt{N_{++}^{\mathrm{same}} \cdot N_{--}^{\mathrm{same}}}}{\sqrt{N_{++}^{\mathrm{mix}} \cdot N_{--}^{\mathrm{mix}}}}. \tag{1}$$

Mixed-event dimuons are required to come from two separate events with a z-vertex difference no larger than 1.5 cm and a difference between collision centrality percentiles that is no larger than 5%. Accumulated mixed-event dimuon counts are five times larger than the same-event dimuons to reduce background statistical uncertainties. The number of selected J/ψ decays inside the dimuon invariant mass $2.8 < m_{\mu\mu}[\mathrm{GeV/c^2}] < 3.5$, the signal over background, after all quality cuts, and the fraction of correlated continuum background f_{cont} are listed in Table II.

Correlated background expected to contribute in the J/ψ mass region is mainly from $c\bar{c} + X \to \mu^+\mu^- + X$ and $b\bar{b} + X \to \mu^+\mu^- + X$ processes. The amount of correlated background shown as dashed lines in Fig. 3 is estimated by fitting the function

$$f_{\mu^+\mu^-}(m) = \mathrm{CBG}(m) + N_{\mathrm{corr}} f_{\mathrm{corr}}(m)$$
$$+ N_{J/\psi} f_{J/\psi}(m) + N_{\psi'} f_{\psi'}(m),$$
$$f_{\mathrm{corr}}(m) = A\varepsilon(m)[c_{\mathrm{lm}} e^{-m/\lambda_{lm}} + (1 - c_{\mathrm{lm}}) m^{-\lambda_{hm}}] \tag{2}$$

to the unlike-sign dimuon mass distribution m, where $\mathrm{CBG}(m)$ is the combinatorial background, $f_{\mathrm{corr}}(m)$ is the correlated background, $f_{J/\psi}(m)$ and $f_{\psi'}$ are the J/ψ and ψ' simulated peaks, $A\varepsilon(m)$ is the mass-dependent detector acceptance and

efficiency determined from simulation and trigger emulator. The correlated background functional form of $f_{\mathrm{corr}}(m)$ accounts for an exponential behavior at low mass and a power-law behavior at high mass, verified in PYTHIA8 simulation of $c\bar{c}$ and $b\bar{b}$ pair production. The free parameters in the fit are N_{corr}, $N_{J/\psi}$, $N_{\psi'}$, c_{lm}, λ_{lm}, and λ_{hm}. Fitting constrains are applied to c_{lm}, λ_{lm}, and λ_{hm} according to a $f_{\mathrm{corr}}(m)$ fit to correlated like-sign dimuon mass distribution in the same mass range. Table II also shows the extracted fractions of correlated background in the J/ψ mass region:

$$f_{\mathrm{cont}} = \int_{m=2.8}^{3.5} dm\, N_{\mathrm{corr}} f_{\mathrm{corr}}(m). \tag{3}$$

B. FVTX-MuTr track association

Requirements for stand-alone FVTX track selection include a minimum of three hits in different FVTX or VTX planes. The analysis requires a FVTX track has a χ^2 probability (p value) larger than 5%. The track quality selection keeps 95% of the true tracks according to simulations. FVTX-MuTr track matching is performed as follows:

(1) MuTr and FVTX tracks are projected to three z-plane locations: (1) the fourth FVTX disk from the vertex, (2) the middle of the absorber materials in front of the MuTr, and (3) the first MuTr station. Radial (R and p_R) and azimuthal (ϕ and p_ϕ) position and momentum projections, and uncertainties ($\sigma_{R_{\mathrm{FVTX-MuTr}}}$, $\sigma_{\phi_{\mathrm{FVTX-MuTr}}}$, $\sigma_{p_{R_{\mathrm{FVTX-MuTr}}}}$, $\sigma_{p_{\phi_{\mathrm{FVTX-MuTr}}}}$) are calculated for each FVTX and MuTr track using the GEANE Kalman Filter algorithm [24], taking into account the detector geometry, the amount of absorber material, and the magnetic field map. The momentum magnitude used for FVTX track projections is taken from the associated MuTr track.

(2) A combined FVTX + MuTr track χ^2 is calculated for each association from individual χ^2_{FVTX} and χ^2_{MuTr} track qualities and FVTX-MuTr projection residuals in the tree planes in an approximation considering the correlation between residuals in different planes is small:

$$\chi^2 = \chi^2_{\mathrm{FVTX}} + \chi^2_{\mathrm{MuTr}} + \chi^2_{\mathrm{match}},$$
$$\chi^2_{\mathrm{match}} = \sum_{i=1}^{3} \frac{\left(R_i^{\mathrm{FVTX}} - R_i^{\mathrm{MuTr}}\right)^2}{\sigma R^2_{\mathrm{FVTX-MuTr}}} + \frac{\left(\phi_i^{\mathrm{FVTX}} - \phi_i^{\mathrm{MuTr}}\right)^2}{\sigma \phi^2_{\mathrm{FVTX-MuTr}}}$$
$$+ \frac{\left(pr_i^{\mathrm{FVTX}} - pr_i^{\mathrm{MuTr}}\right)^2}{\sigma pr^2_{\mathrm{FVTX-MuTr}}}$$
$$+ \frac{\left(p\phi_i^{\mathrm{FVTX}} - p\phi_i^{\mathrm{MuTr}}\right)^2}{\sigma p\phi^2_{\mathrm{FVTX-MuTr}}}, \tag{4}$$

where $p\phi_i^{\mathrm{FVTX}}$ and pr_i^{FVTX} are just track directions determined by the FVTX.

(3) Only FVTX-MuTr combined tracks with $\chi^2/\mathrm{NDF} < 6(3)$ are accepted for further analysis in $p + p$ (Cu+Au) data.

(4) In the $p + p$ analysis, at least one VTX hit is required for tracks inside the VTX acceptance to reduce effects
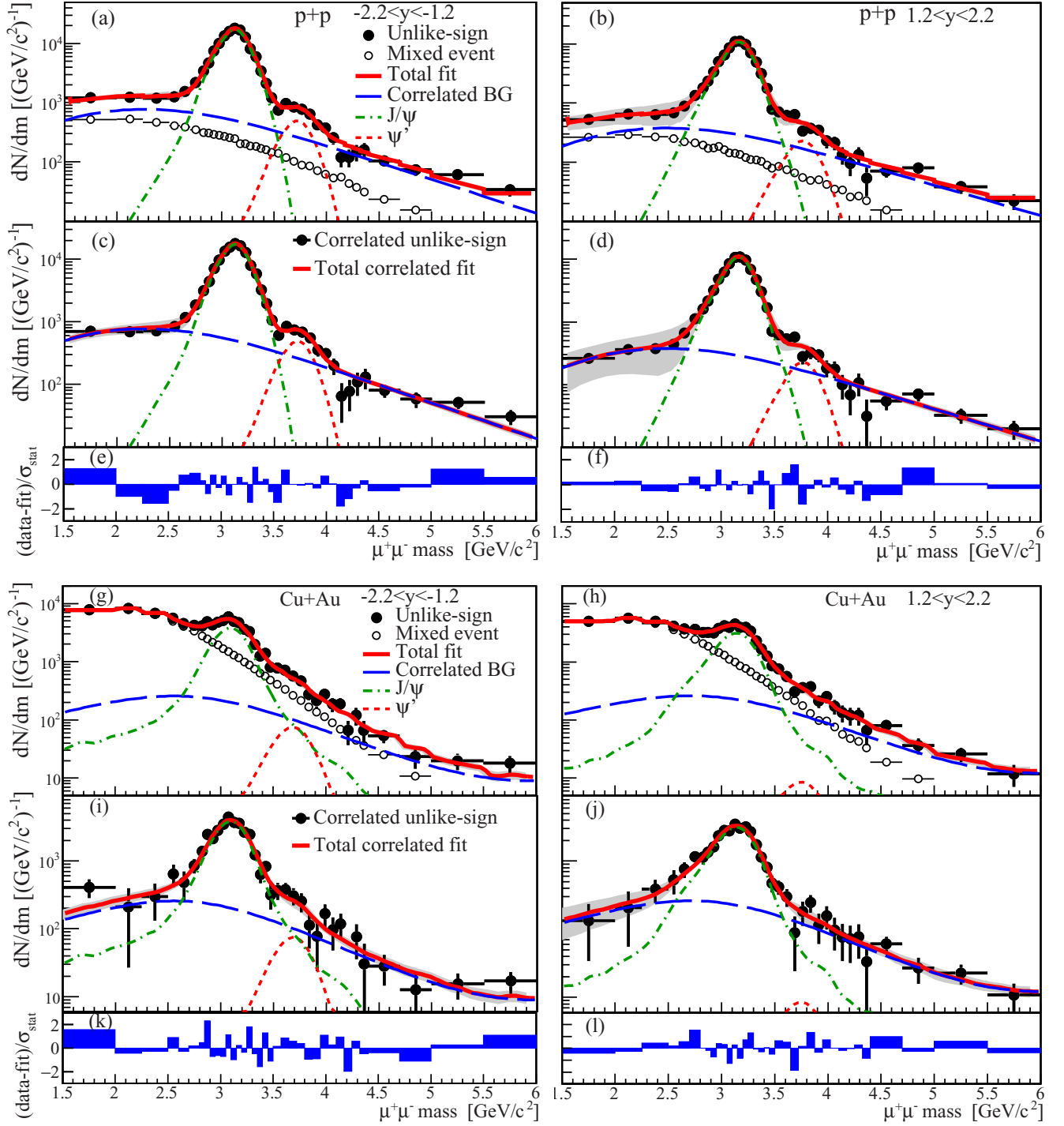
FIG. 3. The dimuon mass distributions in $p + p$ (a)–(f) and Cu+Au (g)–(l) collisions. The mass distribution along with mixed-event dimuons which account for the combinatorial background is shown in panels (a), (b), (g), (h). The distribution after removal of the combinatorial background is shown in panels (c), (d), (i), (j). The lines represent the Eq. (2) components fit to the data points. Panels (e), (f), (k), (l) show the pull between data and fit.

from additional material that was installed just before the 2015 run between the VTX and FVTX.

FVTX-MuTr track mismatches can occur if MuTr tracks are projected onto a region where the FVTX is not active. These MuTr tracks tend to incorrectly associate with tracks

in neighboring live regions which can distort the DCA$_R$ distributions. Fiducial cuts were applied to remove MuTr track projections onto nonactive ϕ regions in the FVTX and their edges to minimize these mismatches. Edge effects are further reduced by requiring the azimuthal residual between the FVTX and MuTr track projections is no larger than

TABLE II. Dimuon net counts, signal to combinatorial background (S/CBG), and the correlated background contribution f_{cont} in the J/ψ mass region $2.8 < m_{\mu\mu}[\text{GeV}/\text{c}^2] < 3.5$.

Data	Arm	Net count	S/CBG	f_{cont}
$p+p$	South	5978 ± 150	32.7	$5.5 \pm 0.3\%$
$p+p$	North	3714 ± 67	33.6	$5.3 \pm 0.4\%$
Cu+Au	South	3075 ± 92	1.13	$10.3 \pm 2.4\%$
Cu+Au	North	2675 ± 82	1.35	$10.7 \pm 2.5\%$

100 mrad (corresponding to the MuTr azimuthal projection resolution).

Once the FVTX-MuTr association passes the matching criteria, the tracks are combined providing a momentum vector and projection at the vertex plane. The combined track has precise momentum and azimuthal direction mostly from the MuTr track information, and FVTX track information dominates the radial direction precision.

We determined that 65% of MuTr tracks in Cu+Au collisions find more than one potential FVTX track association passing the χ^2 quality and the matching criteria described above (Fig. 4), whereas the probability of having more than one association is about 15% in $p+p$ collisions. Because of this small fraction, the $p+p$ analysis uses only the best matching. The multiple associations are pronounced in central Cu+Au events because of the large FVTX track density, and for MuTr tracks with small momentum where projection uncertainties are larger because of the estimated multiple scattering in the absorber. In $B \to J/\psi \to \mu\mu$ events, the best χ^2 association has a chance to happen between a MuTr track from the candidate muon and an FVTX track from an underlying event particle. In this situation, the measured vertex displacement will correspond to a background particle and not the B-meson decay. In the Cu+Au analysis, all FVTX-MuTr associations passing matching criteria (not just the best) are used in the DCA$_R$ distributions to extract the correct FVTX and MuTr track associations. The contribution of mismatches to the track associations is then determined from event mixing, where MuTr tracks from one collision event are mixed with FVTX tracks from another event. Collisions are categorized in 10 FVTX track multiplicity and 200 z-vertex classes. The number of classes was chosen as the minimum number for which there was no observed change in the DCA$_R$ distributions of simulations embedded in real data. MuTr tracks are mixed only with FVTX tracks belonging to the same collision event category. DCA distributions from mismatches are normalized
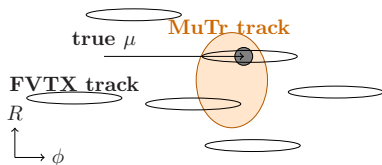

FIG. 4. MuTr (filled ellipse) and FVTX track (open ellipses) projection uncertainty areas at one of the FVTX planes along with the true particle (filled circle).

by the relative FVTX track densities between same-event and mixed-event associations:

$$\text{Norm}_{mis} = \frac{\text{N FVTX tracks in same event}}{\text{N FVTX tracks in mixed events}}. \quad (5)$$

The number of mixed-event FVTX-MuTr associations is arbitrarily chosen to be five times larger than in same events to reduce background statistical fluctuations. The normalization 5 was tested with entire PYTHIA8+GEANT4 events containing prompt J/ψ and $B \to J/\psi$ embedded in real data, where the DCA$_R$ distributions, after subtracting the normalized, event-mixed mismatch tracks, show excellent agreement with DCA$_R$ distributions not embedded in real data.

C. Primary vertex determination

The $p+p$ (Cu+Au) collision events are distributed in a volume, $\sigma_x \times \sigma_y \times \sigma_z$, of approximately $130\,\mu\text{m} \times 130\,\mu\text{m} \times 40\,\text{cm}$ ($90\,\mu\text{m} \times 90\,\mu\text{m} \times 40\,\text{cm}$) centered within the PHENIX detector. Collisions within $z = \pm 10\,\text{cm}$ produce charged particle tracks in the nominal VTX and FVTX acceptance where the tracking can be utilized to precisely determine the collision point. The primary vertex location is found by the minimization of the squared impact parameter for the collection of reconstructed charged particle tracks found in the VTX and the FVTX. In Cu+Au, bias created by tracks with off-vertex decay points is negligible due to the large number of particles created in the collisions of large nuclei and limits on the impact parameter cluster sizes used during the fitting procedure. In Cu+Au, the final primary vertex position is determined by a three dimensional minimization on an event-by-event basis. The majority of the position information in the minimization comes from tracklets within the VTX layers due to this detector's fine azimuthal segmentation of $50\,\mu\text{m}$, short projection length of $\sim 2.6\,\text{cm}$, and typically large impact angles between reconstructed tracks. The event multiplicity is the key factor driving variance in the vertex resolution,

$$\sigma_{\text{VTX}} = \sqrt{\sigma_{\text{VTX}x}^2 + \sigma_{\text{VTX}y}^2 + \sigma_{\text{VTX}z}^2}, \quad (6)$$

where the $\sigma_{\text{VTX}x}$, $\sigma_{\text{VTX}y}$, and $\sigma_{\text{VTX}z}$ vertex uncertainties are obtained event-by-event from the vertex minimization procedure. The vertex uncertainty is determined from independent measurements in north, south, east and west parts of the VTX and FVTX detector. A check of these uncertainties is performed with detector simulation, using HIJING [25] and PYTHIA8 generated events. The σ_{VTX} vertex resolution varies between $30\,\mu\text{m}$ (central collisions) and $200\,\mu\text{m}$ (peripheral collisions) in Cu+Au collisions. Due to the low multiplicity in $p+p$ collisions, the average x and y beam position in

TABLE III. List of vertex position requirements for event selection.

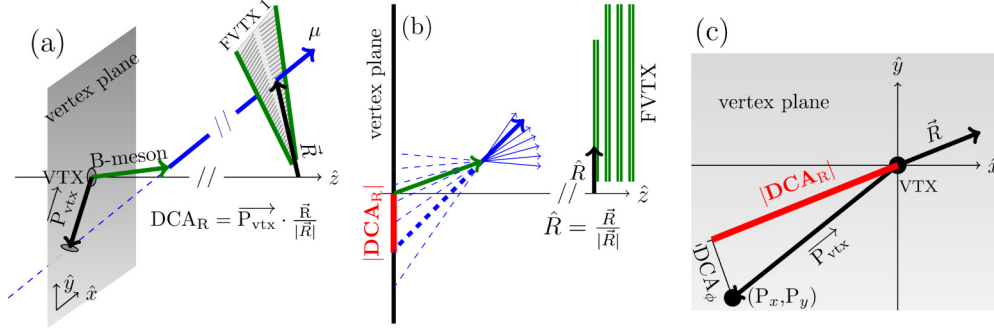| Requirement	Cut
z vertex position range	$|z| < 10\,\text{cm}$
Vertex resolution in $p+p$	$\sigma_Z < 500\,\mu\text{m}$
Vertex resolution in Cu+Au	$\sqrt{\sigma_X^2 + \sigma_Y^2 + \sigma_Z^2} < 200\,\mu\text{m}$

FIG. 5. Visual definition of the displaced vertex DCA_R used in this analysis: (a) 3D, (b) *r*-*z*, and (c) *x*-*y* views. The collision point VTX is at the origin in this view for simplicity.

the transverse plane at the interaction point over a short data taking period ($\sim$90 min) are used in place of an event-by-event determination. Therefore, the *x* and *y* beam position resolutions correspond to the spread of the beam position (130 μm). The *z* position is still determined event-by-event with typical resolution of 200 μm. A summary of all vertex requirements for an event to be selected is listed in Table III.

D. Distance of closest approach measurement

The combined FVTX + MuTr track is projected to a plane perpendicular to the *z* axis and placed at the measured *z* position of the collision point. The displaced vertex vector $\vec{P}_{vtx}$ is defined by the track projection (x_{track}, y_{track}, z_{vtx}) and the collision point (x_{vtx}, y_{vtx}, z_{vtx}) as illustrated in Figs. 5(a) and 5(c).

This projection is not precise in the ϕ direction because of the coarse segmentation of the FVTX in this direction, so the radial projection is used in this analysis, where the FVTX has the best segmentation. In Fig. 5 the radial axis $\vec{R}$ is defined by the track projection at the first FVTX station (x_{FVTX1}, y_{FVTX1}, z_{FVTX1}) and the *z* axis (0, 0, z_{FVTX1}). The precise displacement vertex, which we call the radial distance of closest approach at the vertex plane DCA_R is a projection of the vector $\vec{P}_{vtx}$ on the radial direction $\vec{R}$:

$$DCA_R = \vec{P}_{vtx} \cdot \frac{\vec{R}}{|\vec{R}|}. \qquad (7)$$

Figure 5(b) shows a two-dimensional projection on the *r*-*z* plane of the track. The extension of the DCA_R distribution depends on the decay length of the parent particle and the rapidity difference between the parent particle and the muon. Figure 6 shows the shape of DCA_R distributions of muons from simulated $B \rightarrow J/\psi$ and prompt J/ψ decays thrown in the detector response simulation. Negative DCA_R (where $\vec{P}_{vtx}$ and $\vec{R}$ have opposite directions) is larger for long range decays, producing an asymmetric DCA_R distributions for muons from heavy flavor decays which facilitates their separation from other contributions from prompt particles during the fitting procedure.

E. Backgrounds in the DCA_R distributions

The DCA_R distributions comprise MuTr tracks, from dimuons in the J/ψ mass region, which are associated with

one or more FVTX tracks. Each FVTX + MuTr association counts in the DCA_R distributions. There are two significant sources of uncorrelated background in the DCA_R distributions: (1) combinatorial background described in Sec. III A in the J/ψ mass region, corresponding to dimuons which are not from J/ψ decays; and (2) FVTX-MuTr mismatches described in Sec. III B corresponding to MuTr tracks from J/ψ decays but associated to the wrong FVTX track. Figure 7 shows the contribution of these backgrounds, extracted using the techniques described above, in the raw DCA_R distribution obtained in both arms. The combinatorial background distribution is obtained from mixed-event dimuons, and the mismatch contribution is determined from event mixed MuTr-FVTX associations. Statistical fluctuations are reduced by obtaining five times as many mixed-event pairs and misassociations than in same-event backgrounds. The normalization of these two distributions was explained in Secs. III A and III B. According to the distributions shown in Fig. 7, most background
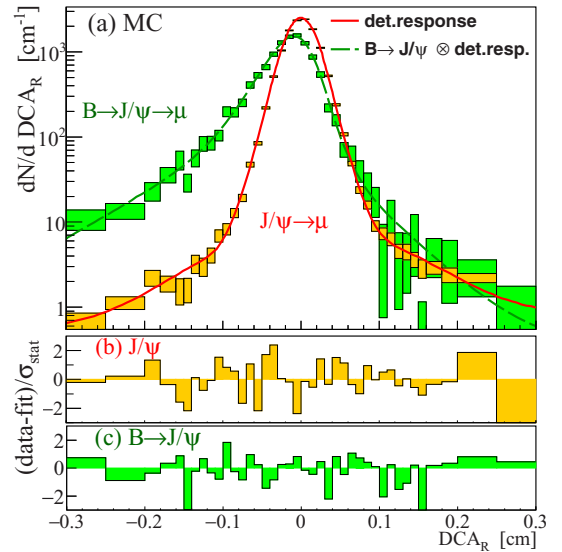

FIG. 6. (a) DCA_R distribution of PYTHIA8+GEANT4 simulated prompt J/ψ and $B \rightarrow J/\psi$ samples as described in Sec. IV (boxes) along with fitted functions Eqs. (9) and (12), respectively. Boxes represent the bin widths and statistical uncertainties in simulation. (b), (c) Pulls between data points from simulation and fitted functions.
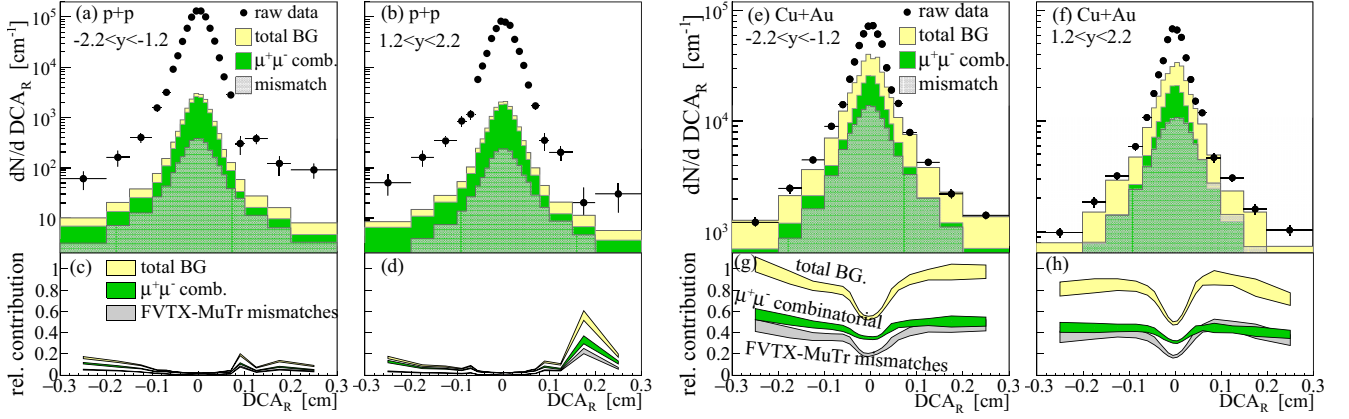
FIG. 7. (a), (b), (e), (f) Uncorrelated background contributions to the DCA$_R$ distributions from $p + p$ (a), (b) and Cu+Au (e), (f) data. (c), (d), (g), (h) Background contribution relative to total yield. Bands in the relative contributions correspond to statistical uncertainties.

contributions come from prompt particles, but the relative background contribution changes at large $|\mathrm{DCA_R}|$, where fake or bad quality tracks and muons from light hadron decays are more significant.

The DCA$_R$ line shape of correlated background contributions from $c\bar{c}$ and $b\bar{b}$ is obtained from simulation and discussed in Sec. IV B.

IV. SIMULATION

In this section we describe how the DCA$_R$ line shape of each dimuon source in the J/ψ mass region is obtained from simulation.

A. Detector response of prompt particles

The detector response to prompt decays, such as muons from prompt J/ψ, is estimated using prompt hadrons (pions, kaons, and protons) generated by the PYTHIA8 event generator in MB mode and a GEANT4-based detector simulation package [26]. Several dead channel configurations are used to account for run-by-run detector acceptance fluctuations. This procedure was found to be crucial to simulate remaining edge effects (Sec. III B) and degradation of FVTX-VTX track quality, which can potentially produce long tails in the measured DCA$_R$ distributions. The simulated GEANT4 signals from all generated hadrons in a single PYTHIA8 event are embedded in real data to account for occupancy and accidental hit-track-association effects in the DCA$_R$ measurement. All particles generated by the detector simulation are shifted by $(\delta x, \delta y, \delta z)$, where each of the coordinates is a common Gaussian random number centered at the vertex position measured in the real data event and with a width determined from the vertex uncertainty of the real event the simulated particles are embedded in. Event reconstruction, including the simulated hits and the entire real data signal in the event, is then performed in the same manner as with real data.

Additional smearing and offsets are needed in the simulated DCA$_R$ to account for irreducible detector misalignments, additional smearing of the primary vertex resolution that is not accounted for in the simulations, and any missing

materials in the simulation that could be a multiple scattering source between the interaction region and the last FVTX plane. The measured DCA$_R$ resolution depends on (1) the vertex uncertainty σ_{VTX} defined in Eq. (6); (2) a momentum-independent parameter σ_a, which represents the sum of the detector resolution contribution to the DCA$_R$ resolution, additional vertex uncertainty which might not be captured by σ_{VTX}, residual detector misalignments and possible beam line tilt variations during the run; and (3) a multiple scattering term σ_b in the VTX and FVTX material which introduces the momentum dependence in the resolution:

$$\sigma_{\mathrm{DCA_R}}(p,\sigma_{\mathrm{vtx}}) = \sqrt{\sigma_{\mathrm{vtx}}^2 + \sigma_a^2 + (\sigma_b/p)^2}. \qquad (8)$$

Particles that stop at the third absorber plane in the MuID comprise mainly prompt light hadrons and ~7% contribution from hadron $\rightarrow \mu$ decays according to PYTHIA8+GEANT4 simulation. This sample provides a relatively clean selection of prompt particles which can be used to compare DCA$_R$ spectra between simulation and real data. The DCA$_R$ distributions from the measured prompt hadrons are compared to simulated hadrons, and small smearing corrections are added to the simulated spectra until they match the real data spectra.

For real data and simulations, the σ_{VTX} value is set according to the event-by-event vertex resolution that is provided by the vertex finding code. The fit parameters σ_a and σ_b are extracted from the real data distributions, and the simulated data has additional smearing added until the distributions produce the same σ_a and σ_b fit results. An additional smearing of 70(110) μm was found to be necessary in the $p + p$ (Cu+Au) setup. After tuning the simulation, the DCA$_R$ distribution of simulated hadrons stopping in the MuID is weighted according to the momentum distribution of real data stopped hadrons.

Figure 8 shows the DCA$_R$ distribution of these prompt hadrons in real data compared to PYTHIA8-generated hadron events, which have had tuned smearing parameters added. Figure 8 also shows the final fit parameters σ_a and σ_b for each of the north (positive rapidity) and south (negative rapidity) arms. Although the material present in the north and south arms is nominally identical, the momentum-dependent
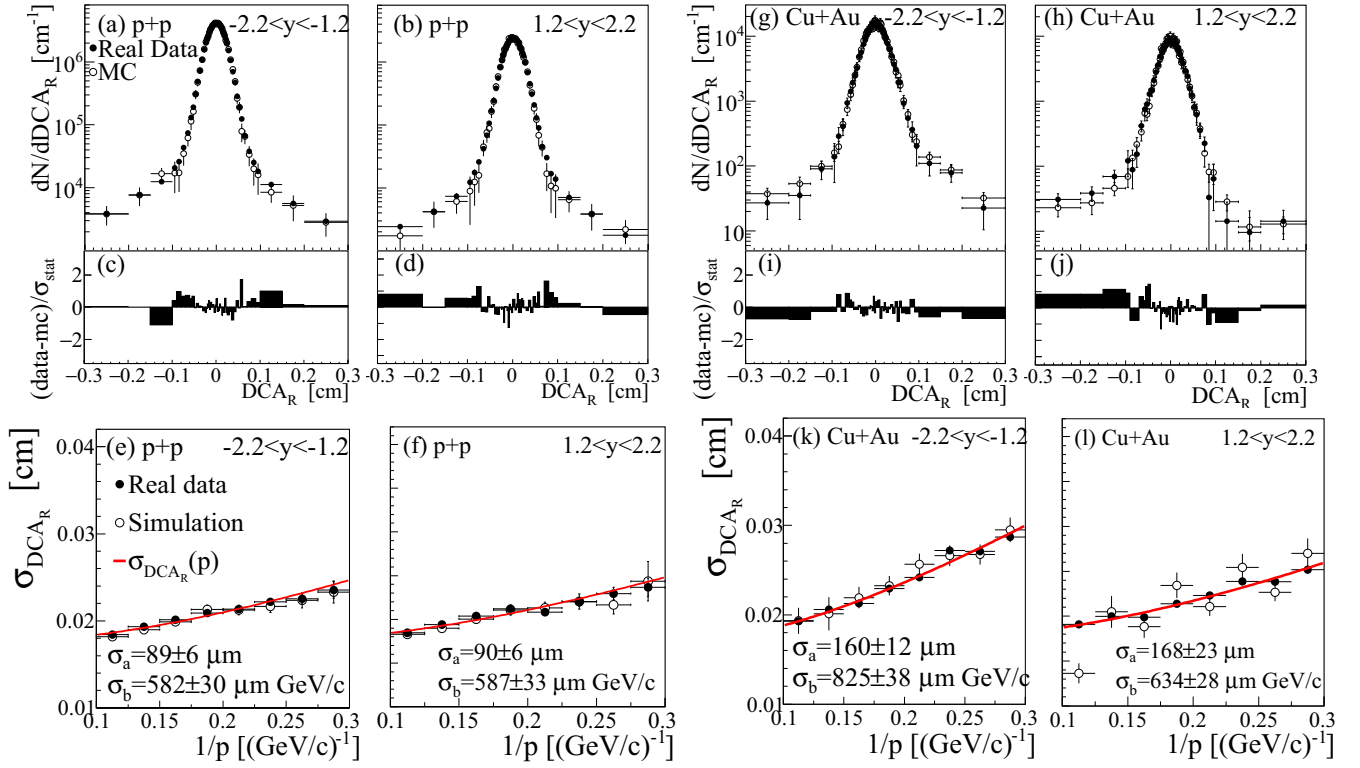
FIG. 8. DCA_R distribution of light hadrons in (a), (b) $p + p$ and (g), (h) Cu+Au real data after (closed circles) FVTX-MuTr mismatch subtraction. (open circles) momentum weighted simulation. (c), (d), (i), (j) Pulls between real data and simulation. (e), (f), (k), (l) Momentum dependence of $DCA_R \in [-0.04, 0.04]$ cm width in real and simulated hadron data along with fitted function Eq. (8).

resolution parameter σ_b is found to be different for the two arms in the Cu+Au data set. The reason for this is that the vertex distribution for BBC-triggered events in Cu+Au events was found to be highly skewed toward the north arm, given the collision species asymmetry. Because of this, FVTX tracks had on average a shorter projection to the vertex for tracks in the north arm than in the south arm, resulting in a smaller contribution to the DCA_R resolution from multiple scattering in the north than in the south. Long tails in the DCA_R distribution contain part of the light hadron decay contribution but are mostly dominated by accidental hit-track associations, which are reasonably well reproduced by the embedded simulation in the DCA_R range used in this analysis.

B. Prompt J/ψ and heavy flavor decay simulations

Prompt J/ψ and $B \to J/\psi$ decays are generated using the PYTHIA8 event generator; open heavy flavor from $c\bar{c}$ and $b\bar{b}$ processes are produced with leading order processes (gluon fusion) and the CT10 parton density distribution functions [27]. All particles generated in the $B \to J/\psi$ or prompt J/ψ event are used as input to the GEANT4 detector simulation and are embedded in real data. Generated events have the DCA_R values smeared and offset according to the parameters obtained for light hadrons as described in Sec. IV A. Simulated events are also weighted according to the momentum distribution of background-subtracted (combinatorial dimuon and FVTX-MuTr mismatch) muons from real data dimuons. Figure 6 shows the DCA_R distributions obtained from these

prompt J/ψ and $B \to J/\psi$ simulations. Several hypotheses of $B \to J/\psi$ nuclear modifications are considered in the momentum weighting for systematic uncertainty evaluations and described in Sec. VI A 2. Point-to-point statistical fluctuations in the generated DCA_R distributions are minimized by using fitted analytical functions for the final DCA_R fits. The DCA_R distributions obtained from prompt J/ψ simulation are well described by a three-Gaussian (G_1, G_2, and G_3) function with a detector offset and resolutions σ_1, σ_2, and σ_3, and regulated by $f_1 + f_2 + f_3 = 1$:

$$\frac{\text{det.resp}(DCA_R)}{N} = f_1 G_1(DCA_R; \text{offset}, \sigma_1)$$
$$+ f_2 G_2(DCA_R; (dca0_2 - \text{offset}), \sigma_2)$$
$$+ f_3 G_3(DCA_R; (dca0_3 - \text{offset}), \sigma_3).$$

(9)

The following function defines the prompt J/ψ DCA_R line shape of prompt J/ψ decays

$$\text{decay}_{J/\psi}(DCA_R) = \delta(0) \otimes \text{det.resp}(DCA_R). \quad (10)$$

The true DCA_R distribution for heavy flavor decays is described by a set of three exponential functions:

$$\text{decay}^{\text{true}}(DCA_R) = \begin{cases} \text{fd}_1 e^{\frac{-DCA_R}{\lambda_{l1}}} + \text{fd}_2 e^{\frac{-DCA_R}{\lambda_{l2}}} & DCA_R < 0 \\ (1 - \text{fd}_1 - \text{fd}_2)e^{\frac{-DCA_R}{\lambda_r}} & DCA_R > 0 \end{cases},$$
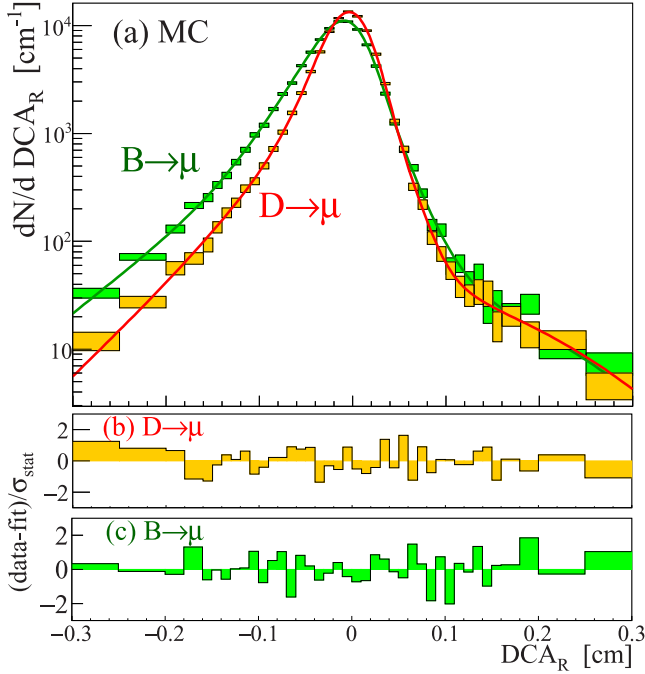
(11)

FIG. 9. (a) Simulated correlated background components, in the dimuon mass $\in$ [2.9,3.5] GeV/c^2, after momentum weighting and vertex uncertainty along with fitted function Eq. (12). Boxes represent the bin widths and statistical uncertainties in simulation. (b), (c) Pulls between simulated data points and fitted functions.

which must be convoluted with the detector response function Eq. (9) extracted from the prompt J/ψ fit to obtain the measured DCA$_R$ distribution:

$$\text{decay}(\text{DCA}_R) = \text{decay}^{\text{true}}(\text{DCA}_R) \otimes \text{det.resp}(\text{DCA}_R). \quad (12)$$

The dashed line in Fig. 6 shows function Eq. (12) fitted to the simulated $B \rightarrow J/\psi$ decays. Function Eq. (12) is also used to fit the simulated correlated background components $c\bar{c}$ and $b\bar{b}$ as seen in Fig. 9. The heavy flavor decay functions used in the final fit are

$$\text{decay}_D(\text{DCA}_R) = \text{decay}(\text{DCA}_R; \overrightarrow{\text{par}}_{D \rightarrow \mu}),$$
$$\text{decay}_B(\text{DCA}_R) = \text{decay}(\text{DCA}_R; \overrightarrow{\text{par}}_{B \rightarrow \mu}), \quad (13)$$
$$\text{decay}_{B \rightarrow J/\psi}(\text{DCA}_R) = \text{decay}(\text{DCA}_R; \overrightarrow{\text{par}}_{B \rightarrow J/\psi \rightarrow \mu}),$$

where $\overrightarrow{\text{par}}_{D \rightarrow \mu}$, $\overrightarrow{\text{par}}_{B \rightarrow \mu}$, and $\overrightarrow{\text{par}}_{B \rightarrow J/\psi \rightarrow \mu}$ are the parameters in Eq. (11) fitted to the corresponding heavy flavor decay simulations.

V. FITTING PROCEDURE

The final fitting function used for the real-data muon DCA$_R$ distribution is

$$f_\mu(\text{DCA}_R) = \text{BG}_{\text{uncor}}(\text{DCA}_R) + \text{BG}_{\text{corr}}(\text{DCA}_R)$$
$$+ N_{J/\psi}\Big[\big(1 - F_{B \rightarrow J/\psi}^{\text{meas}}\big)\text{decay}_{J/\psi}(\text{DCA}_R)$$
$$+ F_{B \rightarrow J/\psi}^{\text{meas}} \cdot \text{decay}_{B \rightarrow J/\psi}(\text{DCA}_R)\Big], \quad (14)$$

where BG$_{\text{uncorr}}$ includes the normalized dimuon combinatorial (Sec. III A) and FVTX-MuTr mismatch (Sec. III B) backgrounds. The correlated background BG$_{\text{corr}}$ comprises $c\bar{c}$ and $b\bar{b}$ contributions:

$$\text{BG}_{\text{corr}}(\text{DCA}_R) = N_{\text{corr}} f_{\text{cont}}[(1 - f_{b\bar{b}})\text{decay}_D(\text{DCA}_R)$$
$$+ f_{b\bar{b}}\text{decay}_B(\text{DCA}_R)],$$

where N_{corr} is the number of muons after subtracting BG$_{\text{uncorr}}$. The continuum correlated background f_{cont} is defined in Table II. The muon count from inclusive J/ψ decays is $N_{J/\psi} = (1 - f_{\text{cont}})N_{\text{corr}}$. The fraction of $b\bar{b}$ contribution in
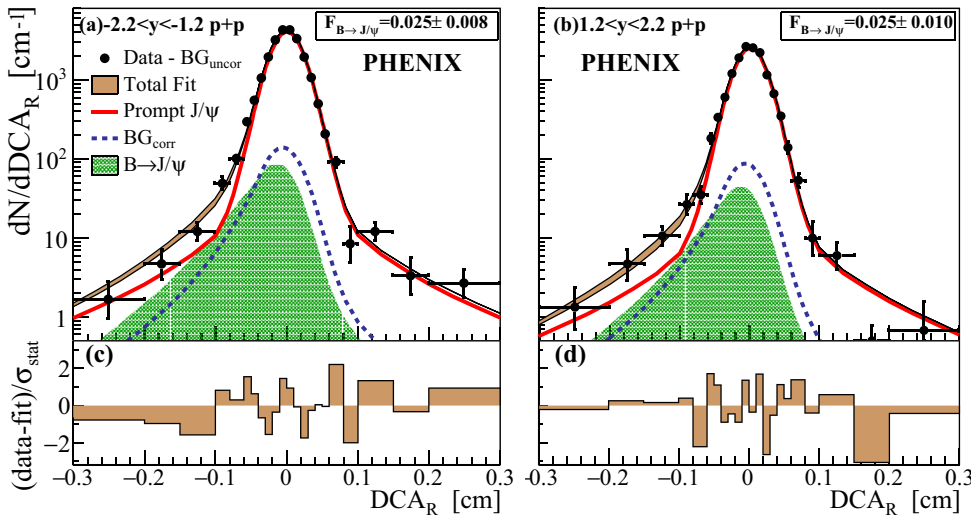

FIG. 10. (a), (b) Function Eq. (14) fitted to the $p + p$ data in different rapidity ranges. The combinatorial and FVTX-MuTr mismatch backgrounds are subtracted from both data and the fitting function for clarity. The band around the total fit curve corresponds to the propagated fitting uncertainty. The resulting F$_{B \rightarrow J/\psi}$ is corrected by the relative acceptance and efficiency, and the evaluated uncertainty is only from the fit. (c), (d) Pulls between data points and fitted functions.
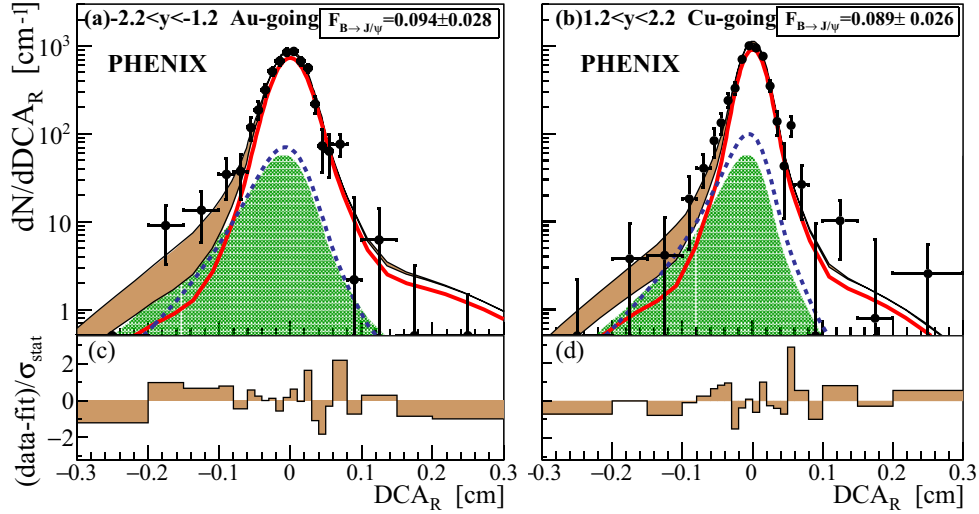
FIG. 11. (a), (b) Function Eq. (14) fitted to the Cu+Au data in different rapidity ranges. The combinatorial and FVTX-MuTr mismatch backgrounds are subtracted from both data and the fitting function for clarity. The band around the total fit curve corresponds to the propagated fitting uncertainty. The resulting $F_{B \to J/\psi}$ is corrected by the relative acceptance and efficiency and the evaluated uncertainty is only from the fit. (c), (d) Pulls between data points and fitted functions.

the correlated background $f_{b\bar{b}}$ was determined from extrapolations of previous $c\bar{c}$ and $b\bar{b}$ cross section measurements [28,29], indicating a fraction $f_{b\bar{b}} = 0.32 \pm 0.21$ in $p + p$ collisions at $\sqrt{s} = 200$ GeV. The $b\bar{b}$ contribution in the correlated background is completely undetermined in Cu+Au collisions. So we set $f_{b\bar{b}} = 0.5$ in the standard fit and vary it in the range $f_{b\bar{b}} \in [0,1]$ for the systematic uncertainty evaluation.

The measured fraction of *B*-meson decays $F_{B \to J/\psi}^{\text{meas}}$ is the only free parameter when fitting function Eq. (14) to the real-data muon DCA$_R$ distribution. The true $F_{B \to J/\psi}$ is obtained by correcting the measured $F_{B \to J/\psi}$ with a factor given by the relative detector acceptance and efficiency of J/ψ from *B*-meson decays with respect to prompt J/ψ decays,

$$\frac{1}{F_{B \to J\psi}} = 1 + \left(\frac{1}{F_{B \to J\psi}^{\text{meas}}} - 1 \right) \frac{\varepsilon_B}{\varepsilon_{J/\psi}}, \quad (15)$$

where $\varepsilon_B / \varepsilon_{J/\psi} \in [0.96, 0.98]$ depending on the data set ($p + p$ or Cu+Au) and muon arm.

The fit is performed with an unbinned extended log-likelihood method, where

$$-\ln \mathcal{L} = \sum_{i=1}^{i=N_\mu} -\ln f_\mu(\text{DCA}_R; F_{B \to J/\psi}) - N_\mu \quad (16)$$

is minimized. N_μ is the number of muons in the DCA$_R$ distribution, including the backgrounds. Figures 10 and 11 show the fitted function Eq. (14) to the DCA$_R$ distributions in $p + p$ and Cu+Au collisions, respectively. The backgrounds due to combinatorial dimuons and FVTX-MuTr mismatches are subtracted for clarity in the figures. The bars in the figure show the total uncertainties of each data point.

VI. SYSTEMATIC UNCERTAINTIES

The systematic uncertainties are determined by fitting $f_\mu(\text{DCA}_R)$ in function Eq. (14) several times, using random

variations of the fitting parameters for each fit. This section lists all considered systematic uncertainty sources and how they affect the final results.

A. List of systematic uncertainty sources

1. Testing of the fitting procedure

The validity of the fitting procedure was tested by randomly generating DCA$_R$ distributions for backgrounds, $B \to J/\psi$, and prompt J/ψ, with $F_{B \to J/\psi}$ tested in the range [0, 0.4]. The total number of entries in the summed DCA$_R$ distributions were generated to match the real data distributions. The
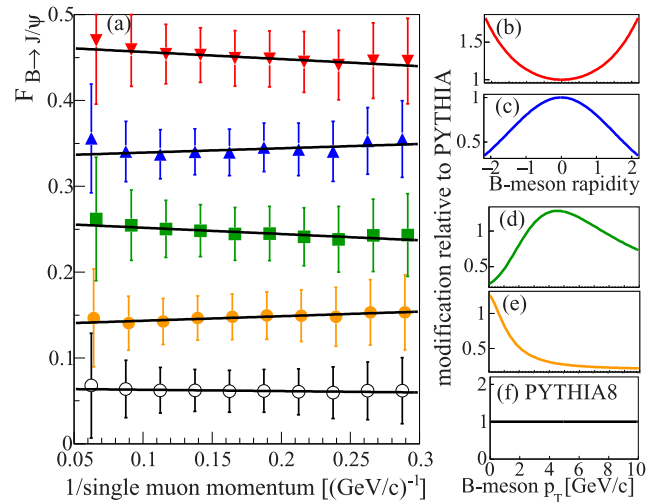

FIG. 12. (a) Momentum distribution of $F_{B \to J/\psi}$ from PYTHIA8 (open circles) and a set of p_T and rapidity *B*-meson yield modifications relative to prompt J/ψ (closed symbols) defined in panels (b)–(f). Scales on $F_{B \to J/\psi}$ are arbitrary.

TABLE IV. Summary of all absolute systematic uncertainties on the $F_{B \to J/\psi}$ measurement.

Source	$p + p$		Cu+Au	
	South	North	South	North
Fitting procedure	<0.001		0.005	0.005
Simulation weighting	0.003	0.002	0.005	0.005
DCA_R resolution	0.004	0.004	0.012	0.015
Detector offset	<0.002		0.011	0.013
DCA_R tail contribution	<0.001		0.002	0.004
Relative acc.×eff.	<0.001		0.005	0.005
Background normalizations	<0.001		0.010	0.009
Correlated bg	0.002	0.003	0.018	0.018
Fraction of corr. $b\bar{b}$	0.008	0.008	0.017	0.018
Total	0.009	0.010	0.033	0.034

fit results over thousands of randomly generated DCA_R distributions in each $F_{B \to J/\psi}^{\text{generated}}$ return $F_{B \to J/\psi}^{\text{measured}}$ with average bias $|F_{B \to J/\psi}^{\text{generated}} - F_{B \to J/\psi}^{\text{measured}}| < 0.005$ in Cu+Au data and negligible in $p + p$ data.

2. Weighting of simulated samples

All detector reconstructed simulated samples were weighted according to the single muon momentum distributions of real data muons from J/ψ decays used in the DCA_R distributions. This weighting already accounts for the realistic momentum distribution of measured dimuons in the J/ψ mass region. Figure 12 shows how the momentum distribution of muons from $B \to J/\psi$ decays are distributed relative to muons from prompt J/ψ decays in several conservative B-meson p_T and rapidity yield modification hypotheses. The inverse momentum dependence obtained from the several hypotheses can be described by polynomials of degree one $f_{B \to J/\psi}(p)$. The maximum deviation from the assumption used in the standard result is $|f_{B \to J/\psi}(p) - F_{B \to J/\psi}| < 0.005$. This value is used in the systematic uncertainty determination.

3. DCA_R resolutions and offsets in simulation

A relative variation of 15% in the detector offset, 5% for σ_a, and 7% for σ_b are found when different fitting ranges are used to determine the offset and the momentum dependence of the DCA_R detector resolution shown in Figs. 8(c), 8(d), 8(g), and 8(h). Varying these parameters within their uncertainties produces fluctuations on the $F_{B \to J/\psi}$ result of up to 0.015.

TABLE V. Fraction of B-meson decays in J/ψ samples obtained in $p + p$ and Cu+Au collisions at $\sqrt{s_{NN}} = 200$ GeV.

Data sample	$F_{B \to J/\psi}$
$-2.2 < y < -1.2 \; p + p$	$0.025 \pm 0.008(\text{stat}) \pm 0.010(\text{syst})$
$1.2 < y < 2.2 \; p + p$	$0.025 \pm 0.010(\text{stat}) \pm 0.009(\text{syst})$
$1.2 < |y| < 2.2 \; p + p$	$0.025 \pm 0.006(\text{stat}) \pm 0.009(\text{syst})$
$-2.2 < y < -1.2$ (Au-going)	$0.094 \pm 0.028(\text{stat}) \pm 0.033(\text{syst})$
$1.2 < y < 2.2$ (Cu+going)	$0.089 \pm 0.026(\text{stat}) \pm 0.034(\text{syst})$

4. DCA_R tail contribution to the detector response function

The detector response function Eq. (9) is fitted to simulated and real data hadrons shown in Fig. 8. The third Gaussian, which accounts for the long range tails in the DCA_R distributions, has a contribution which is 20% different between real and simulated data. This difference can be caused by (1) modified light hadron decay in real data, (2) bias in the FVTX-MuTr mismatch distribution normalization (5); or (3) missing accidental hit-track associations in simulation. The third Gaussian contribution in Eq. (9), f_3, is varied by 20% to account for these uncertainties. This variation produces a change in the $F_{B \to J/\psi}$ of up to 0.004.

5. Relative detector acceptance and efficiency

Variations in the PYTHIA8 parameters, such as renormalization factor and additional weighting to match measured J/ψ rapidity and p_T distributions in Ref. [30], used to determine the relative detector acceptance and efficiency $\varepsilon_B/\varepsilon_{J/\psi}$ introduce 1% relative fluctuation in the $F_{B \to J/\psi}$ result in the $p + p$. When considering different scenarios for the B-meson nuclear modification in Cu+Au; including variations with centrality p_T and rapidity; the fluctuation in $F_{B \to J/\psi}$ relative to the default result is 5%.

6. Dimuon combinatorial background and FVTX-MuTr mismatch distribution normalizations

The dimuon combinatorial background normalization Eq. (1) varies by up to 3% when changing the mass range used to determine it. Another concern is how particle activity surrounding a B meson can affect the normalization Eq. (5) of FVTX-MuTr mismatch distributions. The normalization shows a 5% variation when embedding entire PYTHIA8+GEANT4 events containing prompt J/ψ and $B \to J/\psi$. When applying these variations in the DCA_R fitting Eq. (14), the $F_{B \to J/\psi}$ result has a standard deviation of 0.01.

7. Correlated background

The dimuon mass fitting uncertainty for the correlated background contributions shown in Table II is introduced as Gaussian random numbers before each fit. The fraction of $b\bar{b}$ in the correlated background is varied by $f_{b\bar{b}} = 0.32 \pm 0.21$ in
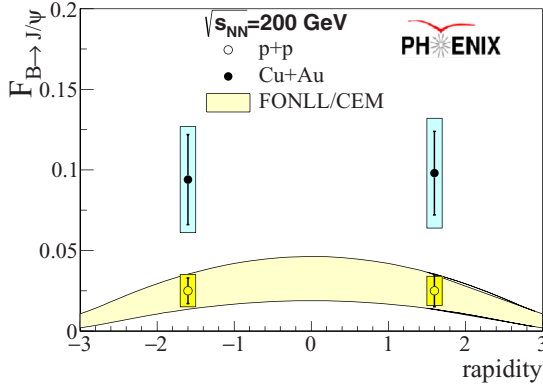
FIG. 13. Fraction $F_{B \to J/\psi}$ of *B*-meson decays in the inclusive J/ψ sample in $p + p$ and Cu+Au collisions at $\sqrt{s_{NN}} = 200$ GeV versus rapidity along with a theoretical estimation based on fixed-order plus next-to-leading logs (FONLL) [31,32] for the $B \to J/\psi$ cross section and color-evaporation-model (CEM) [33] for the prompt J/ψ. The statistical uncertainties are represented by the error bars and the systematic uncertainties are represented by filled boxes.

$p + p$ collisions based on the uncertainties in the total $c\bar{c}$ and $b\bar{b}$ cross section [28,29]. For Cu+Au collisions, $f_{b\bar{b}} \in [0,1]$ is considered, which accounts for unknown $c\bar{c}$ and $b\bar{b}$ nuclear modifications. When applying these variations in the fitting procedure defined in Eq. (14) the $F_{B \to J/\psi}$ standard deviation is 0.01 in $p + p$ and 0.025 in Cu+Au.

B. Total systematic uncertainties

Table IV summarizes all systematic uncertainty contributions. The total systematic uncertainty also listed in the table is obtained by varying the parameters as described in the fitting function Eq. (14) simultaneously, assuming all variations are independent, and running several independent fits.

C. Other checks

Other tests such as variations in the DCA_R fitting range, and the use of simulated histograms rather than functions as fitting input, provided results that are statistically consistent with the default result. No additional systematic uncertainties are assigned from these checks.
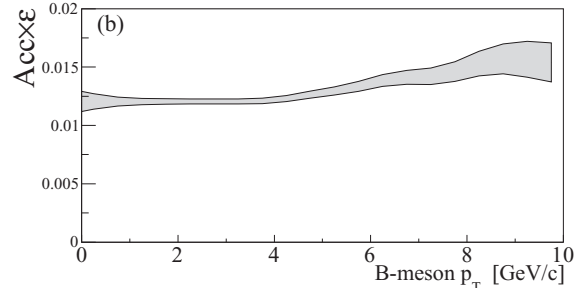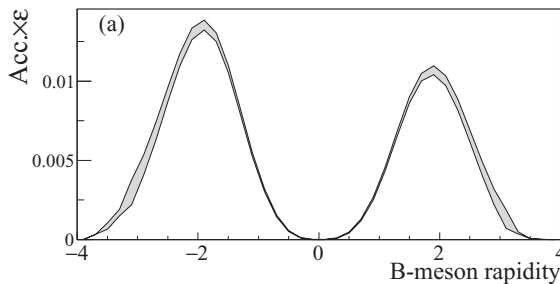
VII. RESULTS

A. Fraction of B mesons in the J/ψ sample

The acceptance and efficiency corrected *B*-meson contributions to the J/ψ yields collected in $p + p$ and Cu+Au data are listed in Table V and plotted in Fig. 13. The detector acceptance and efficiency of *B*-meson decays producing a J/ψ in the muon arm apertures is shown in Fig. 14 as a function of rapidity and transverse momentum. The estimation is obtained from the simulation setup described in Sec. IV embedded in Cu+Au raw data. As can be seen in the right panel, the measurement presented in this analysis is the first which covers B mesons starting from zero p_T in heavy ion collisions.

The $F_{B \to J/\psi}$ obtained in $p + p$ collisions is well described by a theoretical calculation based on FONLL [31,32] for the $B \to J/\psi$ and color-evaporation-Model (CEM) [33] for the prompt J/ψ differential cross sections. Uncertainties in the theoretical calculation come from the bottom quark mass (4.5–5.0 GeV/c^2) and scale uncertainties. The CTEQ6 parton-density function [34] was adopted in both FONLL and CEM calculations.

B. Differential cross section of $b\bar{b}$ in $p + p$ collisions

The corresponding $p + p \to b\bar{b}$ differential cross section can be calculated by

$$\frac{d\sigma_{b\bar{b}}}{dy} = \frac{\frac{1}{2}d\sigma_{J/\psi}/dy \times F_{B \to J/\psi}}{\mathrm{Br}(B \to J/\psi + X)}, \qquad (17)$$

where $d\sigma_{J/\psi}/dy$ is obtained from J/ψ measurement by PHENIX [30]. The branching ratios $\mathrm{Br}(B \to J/\psi + X)$ and $\mathrm{Br}(J/\psi \to \mu^+\mu^-)$ are reported in the particle data group [3]. The factor $\frac{1}{2}$ accounts for the fact that both *b* quarks in the $b\bar{b}$ pair contribute to the $F_{B \to J/\psi}$. The results are shown in Table VI, where the average rapidity $\langle y \rangle$ are obtained from the detector acceptance of $B \to J/\psi$ events generated by PYTHIA8. Table VI also presents the corresponding FONLL calculation.

C. *B*-meson nuclear modification

The nuclear modification factor is defined by

$$R_{CuAu} = \frac{(dN/dy)^{CuAu}}{\langle N_{coll} \rangle (dN/dy)^{pp}}, \qquad (18)$$

where dN/dy is the yield in Cu+Au and $p + p$ collisions and $\langle N_{coll} \rangle$ is the average number of binary collisions in the

FIG. 14. Detector acceptance $\times$ efficiency of *B*-meson decays producing a J/ψ in the muon arms ($1.2 < |y| < 2.2$) versus *B*-meson (a) and rapidity (b) p_T. The statistical uncertainties in simulation are shown in filled gray bands.

TABLE VI. Differential cross section for $p + p \rightarrow b\bar{b}$ at $\sqrt{s} = 200$ GeV obtained from Eq. (17) along with the FONLL theoretical calculation [31,32].

$\langle y \rangle$	$d\sigma_{b\bar{b}}/dy$ [μb]
-1.6	$0.51 \pm 0.16(\text{stat}) \pm 0.20(\text{sys})$
1.6	$0.52 \pm 0.21(\text{stat}) \pm 0.21(\text{sys})$
$|1.6|$	$0.51 \pm 0.13(\text{stat}) \pm 0.20(\text{sys})$
$|1.6|$ (FONLL)	$0.26^{+0.14}_{-0.10}(\text{theory uncert.})$

Cu+Au data sample. The Glauber estimated average number of collisions in Cu+Au collisions is $\langle N_{\text{coll}} \rangle = 108 \pm 11$. The centrality and p_T integrated R_{CuAu} for inclusive J/ψ in Cu+Au collisions is obtained from the results presented in Ref. [17]: $0.365 \pm 0.019(\text{stat}) \pm 0.026(\text{syst})$ in the Au-going direction and $0.295 \pm 0.026(\text{stat}) \pm 0.021(\text{syst})$ in the Cu-going direction with a global uncertainty of 7.1%. The separated prompt J/ψ and B-meson R_{CuAu} can be extracted from inclusive J/ψ R_{CuAu} and $F_{B \rightarrow J/\psi}$ through

$$R_{\text{CuAu}}^{\text{prompt}} = \frac{1 - F_{B \rightarrow J/\psi}^{\text{CuAu}}}{1 - F_{B \rightarrow J/\psi}^{pp}} R_{\text{CuAu}}^{\text{incl.}}, \quad R_{\text{CuAu}}^{B} = \frac{F_{B \rightarrow J/\psi}^{\text{CuAu}}}{F_{B \rightarrow J/\psi}^{pp}} R_{\text{CuAu}}^{\text{incl.}},$$

$$(19)$$

where $R_{\text{CuAu}}^{\text{prompt}}$, R_{CuAu}^{B}, and $R_{\text{CuAu}}^{\text{incl.}}$ are the nuclear modification factors for prompt J/ψ, B mesons and inclusive J/ψ, respectively.

The average of the results for $F_{B \rightarrow J/\psi}$ shown in the first two rows of Table V is used as a $p + p$ reference $F_{B \rightarrow J/\psi}^{pp}$. The uncertainties in the DCA$_R$ resolution in simulation are correlated between the $p + p$ and Cu+Au analysis and cancel out in the R_{CuAu} results. The global uncertainty includes statistical and systematic uncertainties of the $p + p$ reference. Table VII and Fig. 15 summarizes the B-meson and prompt-J/ψ nuclear modifications obtained using Eq. (19).

Both nuclear modifications factors from forward and backward rapidities are consistent with binary scaling of $p + p$ yields given the large uncertainties. The results are also consistent with initial-state effects predicted by the EPS09 model [12], shown in Fig. 15, which suggests a modest enhancement. The EPS09 calculation uses as input x and Q from $gg \rightarrow b\bar{b}$ events generated by PYTHIA8. The same model underpredicts the large yield enhancements observed for leptons from inclusive heavy flavor, dominated by charm quarks, at midrapidity and negative rapidity in $d + $Au collisions [14,15] at the same energy. Heavy flavor yield enhancement

TABLE VII. Nuclear modification factors of B mesons and prompt J/ψ obtained from Eq. (19).

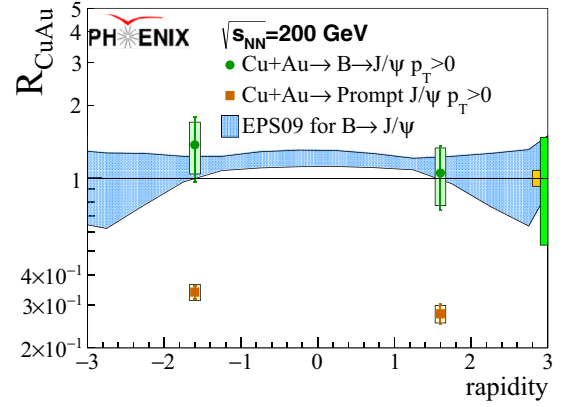|	R_{CuAu}^{B}
Au-going	$1.37 \pm 0.41(\text{stat}) \pm 0.33(\text{syst}) \pm 0.47(\text{pp})$
Cu+going	$1.05 \pm 0.31(\text{stat}) \pm 0.28(\text{syst}) \pm 0.47(\text{pp})$
	$R_{\text{CuAu}}^{\text{prompt}}$
Au-going	$0.339 \pm 0.021(\text{stat}) \pm 0.026(\text{syst}) \pm 0.075(\text{pp})$
Cu+going	$0.276 \pm 0.026(\text{stat}) \pm 0.023(\text{syst}) \pm 0.075(\text{pp})$

FIG. 15. Rapidity dependence of B-meson and prompt-J/ψ meson nuclear modification factors R_{CuAu} along with the initial state effect estimated from EPS09 [12]. The statistical uncertainties are shown as bars, and the systematic uncertainties are shown as filled boxes. The boxes at rapidity=3 are global uncertainties for the prompt J/ψ and $B \rightarrow J/\psi$.

at large-x, which dominates the negative rapidity yield, is also expected from incoherent multiple scattering of initial gluons [9].

Binary scaling of momentum-integrated heavy flavor production was previously observed in electron yields from charm quarks by PHENIX [35] and reconstructed D mesons by STAR [36] in Au + Au collisions at RHIC. The p_T integrated B-meson nuclear modification result obtained in this work, when combined with these earlier results, indicate there is binary scaling of B and D mesons separately. Because charm and bottom number are conserved in heavy ion collisions at $\sqrt{s_{NN}} = 200$ GeV, the interaction with the QGP medium only alters the momentum distribution of D mesons and B mesons causing a relative yield suppression for $p_T \gg m_Q$.

VIII. SUMMARY AND CONCLUSIONS

We report the fraction of B-meson decays in the inclusive J/ψ yield in $p + p$ and Cu+Au collisions at $\sqrt{s_{NN}} = 200$ GeV. The measurement is centrality and p_T integrated with acceptance starting from zero p_T B mesons. The $b\bar{b}$ differential cross section obtained from the measured fractions at rapidity $1.2 < |y| < 2.2$ in $p + p$ collisions is consistent with FONLL theoretical calculation within uncertainties [31,32]. A systematically larger fraction is observed in Cu + Au collisions than in $p + p$ collisions, which reflects a smaller nuclear modification of B mesons in Cu + Au collisions compared to prompt J/ψ. The nuclear modification factor calculated from the Cu + Au and $p + p$ fractions, along with the measured inclusive J/ψ R_{CuAu}, are listed in Table VII and shown in Fig. 15. The results are consistent with binary scaling of B-meson yields. No significant difference is observed between the Cu-going and Au-going direction within the result uncertainties. However, yield enhancement at negative rapidity is favored, which is in agreement with cold-nuclear-matter effects observed for inclusive heavy flavor in $d + $Au collisions at the same energy [14,15], an EPS09-based calculation, and

incoherent multiple scattering of initial gluons. This result and others on charm yields indicate that heavy-quark number is conserved in heavy ion collisions at $\sqrt{s_{NN}} = 200$ GeV. Interaction with the QGP medium only alters momentum distributions of D and B mesons. The nuclear modification observed for B mesons contrasts with the strong suppression measured for prompt J/ψ mesons indicating that final-state effects, where the $c\bar{c}$ binding is broken by the medium formed, are dominant for prompt J/ψ mesons.

[1] J. D. Bjorken, Energy Loss of Energetic Partons in Quark-Gluon Plasma: Possible Extinction of High p(t) Jets in Hadron-Hadron Collisions (1982), FERMILAB-PUB-82-059-THY, FERMILAB-PUB-82-059-T.

[2] Y. L. Dokshitzer and D. E. Kharzeev, Heavy-quark colorimetry of QCD matter, Phys. Lett. B **519**, 199 (2001).

[3] K. A. Olive *et al.* (Particle Data Group), Review of particle physics, Chin. Phys. C **38**, 090001 (2014).

[4] R. Aaij *et al.* (LHCb Collaboration), Measurements of the B^+, B^0, B_s^0 meson and Λ_b^0 baryon lifetimes, J. High Energy Phys. 04 (2014) 114.

[5] E. Norrbin and T. Sjöstrand, Production and hadronization of heavy quarks, Eur. Phys. J. C **17**, 137 (2000).

[6] I. Vitev, T. Goldman, M. B. Johnson, and J. W. Qiu, Open charm tomography of cold nuclear matter, Phys. Rev. D **74**, 054010 (2006).

[7] T. Sjostrand, S. Mrenna, and P. Z. Skands, A Brief Introduction to PYTHIA8.1, Comput. Phys. Commun. **178**, 852 (2008).

[8] Z.-B. Kang, I. Vitev, and H. Xing, Multiple scattering effects on inclusive particle production in the large-x regime, Phys. Rev. D **88**, 054010 (2013).

[9] Z.-B. Kang, I. Vitev, E. Wang, H. Xing, and C. Zhang, Multiple scattering effects on heavy meson production in $p + A$ collisions at backward rapidity, Phys. Lett. B **740**, 23 (2015).

[10] Z.-B. Kang, I. Vitev, and H. Xing, Effects of cold nuclear matter energy loss on inclusive jet production in $p + A$ collisions at energies available at the BNL Relativistic Heavy Ion Collider and the CERN Large Hadron Collider, Phys. Rev. C **92**, 054911 (2015).

[11] L. D. McLerran and R. Venugopalan, Gluon distribution functions for very large nuclei at small transverse momentum, Phys. Rev. D **49**, 3352 (1994).

[12] K. J. Eskola, H. Paukkunen, and C. A. Salgado, EPS09: A New Generation of NLO and LO Nuclear Parton Distribution Functions, J. High Energy Phys. 04 (2009) 065.

[13] I. Helenius, K. J. Eskola, H. Honkanen, and Carlos A. Salgado, Impact-Parameter Dependent Nuclear Parton Distribution Functions: EPS09s and EKS98s and Their Applications in Nuclear Hard Processes, J. High Energy Phys. 07 (2012) 073.

[14] A. Adare *et al.* (PHENIX Collaboration), Cold-Nuclear-Matter Effects on Heavy-Quark Production at Forward and Backward Rapidity in d+Au Collisions at $\sqrt{s_{NN}} = 200$ GeV, Phys. Rev. Lett. **112**, 252301 (2014).

[15] A. Adare *et al.* (PHENIX Collaboration), Cold Nuclear Matter Effects on Heavy-Quark Production in $d + $Au Collisions at $\sqrt{s_{NN}} = 200$ GeV, Phys. Rev. Lett. **109**, 242301 (2012).

[16] J. Adams *et al.* (STAR Collaboration), Open Charm Yields in d+Au Collisions at $\sqrt{s} = 200$ GeV, Phys. Rev. Lett. **94**, 062301 (2005).

[17] C. Aidala *et al.* (PHENIX Collaboration), Nuclear matter effects on J/ψ production in asymmetric Cu+Au collisions at $\sqrt{s_{NN}} = 200$ GeV, Phys. Rev. C **90**, 064908 (2014).

[18] H. Xing, Y. Guo, E. Wang, and X.-N. Wang, Parton energy loss and modified beam quark distribution functions in Drell-Yan process in collisions, Nucl. Phys. A **879**, 77 (2012).

[19] C. Aidala *et al.*, The PHENIX Forward Silicon Vertex Detector, Nucl. Instrum. Methods Phys. Res., Sec. A **755**, 44 (2014).

[20] H. Akikawa *et al.*, PHENIX Muon Arms, Nucl. Instrum. Methods Phys. Res., Sec. A **499**, 537 (2003).

[21] S. S. Adler *et al.* (PHENIX Collaboration), Measurement of single muons at forward rapidity in $p + p$ collisions at $\sqrt{s} = 200$ GeV and implications for charm production, Phys. Rev. D **76**, 092002 (2007).

[22] Z. Li, H. En'yo, Y. Goto, V. Radeka, W. Chen, D. Elliott, T. Kawabata, M. Togawa, N. Saito, V. Rykov, K. Tanida, and

J. Tojo, Novel silicon stripixel detector for PHENIX Upgrade, Nucl. Instrum. Methods Phys. Res., Sec. A **518**, 300 (2004).

[23] R. Ichimiya *et al.*, Status and overview of development of the silicon pixel detector for the phenix experiment at the BNL RHIC, J. Instrum. **4**, P05001 (2009).

[24] V. Innocente, M. Maire, and E. Nagy, GEANE: Average Tracking and Error Propagation Package, July 1991, CERN, IT-ASD W5013-E GEANE.

[25] X.-N. Wang and M. Gyulassy, HIJING: A Monte Carlo model for multiple jet production in pp, pA, and AA collisions, Phys. Rev. D **44**, 3501 (1991).

[26] S. Agostinelli *et al.*, GEANT4-a simulation toolkit, Nucl. Instrum. Methods Phys. Res., Sec. A **506**, 250 (2003).

[27] H.-L. Lai, M. Guzzi, J. Huston, Z. Li, P. M. Nadolsky, J. Pumplin, and C.-P. Yuan, New parton distributions for collider physics, Phys. Rev. D **82**, 074024 (2010).

[28] A. Adare *et al.* (PHENIX Collaboration), Measurement of High-p_T Single Electrons from Heavy-Flavor Decays in $p + p$ Collisions at $\sqrt{s} = 200$ GeV, Phys. Rev. Lett. **97**, 252002 (2006).

[29] A. Adare *et al.* (PHENIX Collaboration), Measurement of Bottom versus Charm as a Function of Transverse Momentum with Electron-Hadron Correlations in $p + p$ Collisions at $\sqrt{s} = 200$ GeV, Phys. Rev. Lett. **103**, 082002 (2009).

[30] A. Adare *et al.* (PHENIX Collaboration), Ground and excited charmonium state production in $p + p$ collisions at $\sqrt{s} = 200$ GeV, Phys. Rev. D **85**, 092004 (2012).

[31] M. Cacciari, M. Greco, and P. Nason, The P(T) spectrum in heavy flavor hadroproduction, J. High Energy Phys. 05 (1998) 007.

[32] M. Cacciari, P. Nason, and R. Vogt, QCD Predictions for Charm and Bottom Production at RHIC, Phys. Rev. Lett. **95**, 122001 (2005).

[33] A. D. Frawley, T. Ullrich, and R. Vogt, Heavy flavor in heavy-ion collisions at RHIC and RHIC II, Phys. Rep. **462**, 125 (2008).

[34] P. M. Nadolsky, H.-L. Lai, Q.-H. Cao, J. Huston, J. Pumplin, D. Stump, W.-K. Tung, and C. P. Yuan, Implications of CTEQ global analysis for collider observables, Phys. Rev. D **78**, 013004 (2008).

[35] A. Adare *et al.* (PHENIX Collaboration), Heavy Quark Production in $p + p$ and Energy Loss and Flow of Heavy Quarks in Au+Au Collisions at $\sqrt{s_{NN}} = 200$ GeV, Phys. Rev. C **84**, 044905 (2011).

[36] L. Adamczyk *et al.* (STAR Collaboration), Observation of D^0 Meson Nuclear Modifications in Au+Au Collisions at $\sqrt{s_{NN}} = 200$ GeV, Phys. Rev. Lett. **113**, 142301 (2014).